Research Square

Preprints are preliminary reports that have not undergone peer review.
They should not be considered conclusive, used to inform clinical practice,
or referenced by the media as validated information.

Inducible Nitric Oxide Synthase (NOS2) is Required for Oligodendrocyte Lineage Progression and Remyelination in Murine β-Coronavirus-Induced Neuroinflammation

Rishika Jana
Indian Institute of Science Education and Research Kolkata
Santosh Kumar Samal
Indian Institute of Science Education and Research Kolkata
Souvik Karmakar
Indian Institute of Science Education and Research Kolkata
Subhajit Das Sarma
Indian Institute of Science Education and Research Kolkata
Jayasri Das Sarma
dassarmaj@iiserkol.ac.in

Indian Institute of Science Education and Research Kolkata

Research Article

Keywords: Demyelination, Remyelination, Inducible nitric oxide synthase (NOS2), β-coronavirus, Neuroinflammation, Oligodendrocyte precursor cells (OPCs), Mature Oligodendrocytes

Posted Date: November 4th, 2026

DOI: https://doi.org/10.21203/rs.3.rs-11610389/v1

License: This work is licensed under a Creative Commons Attribution 4.0 International License.
Read Full License

Additional Declarations: No competing interests reported.

Inducible Nitric Oxide Synthase (NOS2) is Required for Oligodendrocyte Lineage Progression and Remyelination in Murine β-Coronavirus-Induced Neuroinflammation

Rishika Jana[1], Santosh Kumar Samal[1], Souvik Karmakar[1,2], Subhajit Das Sarma[1], Jayasri Das Sarma[1, 3,4*]

1. Department of Biological Sciences, Indian Institute of Science Education and Research, Kolkata, Mohanpur-741246, India

2. Department of Microbiology and Immunology, Carver College of Medicine, Iowa City

3. Department of Ophthalmology, Philadelphia, Pennsylvania, United States of America

4. Centre for Molecular Neurosciences, Kasturba Medical College, MAHE-Manipal

* Corresponding Author - dassarmaj@iiserkol.ac.in

Abstract-

Background: Multiple sclerosis (MS) and post-viral demyelinating encephalomyelitis are characterized by chronic central nervous system (CNS) inflammation, myelin sheath destruction, and impaired tissue repair. While inducible nitric oxide synthase (NOS2) is traditionally viewed as a cytotoxic mediator in acute neuroinflammation, its temporal role, from myelin loss to the long-term endogenous remyelination phase, has remained controversial and poorly defined. Using a murine β-coronavirus (MHV-RSA59) model of neuroinflammation, we investigated the requirement for NOS2 during the myelin loss and repair phase (days 30 to 60 post-infection).

Method: Age-matched C57BL/6 wild-type (WT) and NOS2-/-mice were intracranially inoculated with 10,000 PFU of RSA59. Animals were euthanized at defined time points (day 30 and day 60 post-infection) to harvest the tissue samples. Luxal Fast Blue (LFB) staining, immunofluorescence (IF), immunoblotting, immunohistochemistry, and flow cytometry were performed on the RSA59-infected brain and spinal cord samples of NOS2-/- and WT mice.

Results: Our recent findings revealed that NOS2-/- mice, compared to WT mice, showed persistent demyelinating plaques, reduced myelin restoration, as indicated by the expression of myelin-forming proteins, and a diminution of oligodendrocyte precursor cells (OPCs) and mature oligodendrocytes during the remyelination phase. This delayed regenerative process in the absence of NOS2 was associated with prolonged activation of CNS-resident microglia and

an infiltrated myeloid cell population, which may lead to a dysregulated inflammatory environment in the CNS. Mechanistically, loss of NOS2 led to more phagocytic activity in CNS-resident microglia and infiltrating myeloid cells. Our findings establish that NOS2-derived signals are essential for clearing inflammatory debris and transitioning myeloid cells from a pro-inflammatory state toward a pro-regenerative phenotype, thereby creating a permissive microenvironment for myelin repair.

Conclusion: This study elucidates how NOS2 regulates the balance between pathological damage and tissue repair. Also, our current research highlights NOS2 not merely as a marker of inflammation, but as a crucial protective factor required for effective myelin regeneration in virus-induced neuroinflammatory demyelination.

Keywords: Demyelination, Remyelination, Inducible nitric oxide synthase (NOS2), β-coronavirus, Neuroinflammation, Oligodendrocyte precursor cells (OPCs), Mature Oligodendrocytes.

Introduction:

Multiple sclerosis (MS) is a progressive autoimmune and neurodegenerative disorder of the central nervous system (CNS) characterized by multifocal neuroinflammation, extensive white matter injury, and oligodendrocyte loss[1–4]. The clinical hallmarks of MS include progressive axonal degeneration [5], myelin sheath collapse[6]and the loss of mature myelinating oligodendrocytes [7,8]. These collectively disrupt saltatory conduction and lead to progressive neurological disability[9–11]. Although current disease-modifying therapies primarily focus on suppressing early peripheral immune cell infiltration[12]strategies that stimulate endogenous remyelination have emerged as essential interventions to preserve axonal integrity and restore neurological function[13–16] . However, in MS lesions, the transition from acute neuroinflammatory damage to active tissue repair is frequently delayed or halted. Identifying the molecular regulators that orchestrate this transition from inflammation to repair remains a central goal in the neurobiology of diseases.

CNS neuroinflammation involves the sustained activation of resident microglia and infiltrating leukocytes, which release an array of cytokines, chemokines, reactive oxygen species (ROS), and reactive nitrogen species (RNS) [17–19] . Microglia and macrophages exert a dual role in this landscape: while they mediate early tissue injury, they also provide essential pro-

regenerative functions by clearing myelin debris and secreting neurotrophic factors necessary for remyelination[20–24] . Among the inflammatory effectors produced by these cells, inducible nitric oxide synthase (NOS2) is a key enzyme that converts L-arginine to nitric oxide (NO) [25] . NO exerts complex, context-dependent effects within the CNS. On one hand, NO is an essential component of innate pathogen clearance and viral inhibition; on the other hand, high concentrations of NO can induce oxidative stress, mitochondrial dysfunction, and cytotoxicity in neurons and oligodendrocytes [25–27] .

This dichotomy has fueled decades of debate regarding whether NOS2 acts primarily as a pathogenic driver that must be inhibited or as an essential regulatory checkpoint governing the immune microenvironment. In the cuprizone-induced demyelination model, NOS2 deficiency exacerbates disease severity[28]. In experimental autoimmune encephalomyelitis (EAE), NOS2 exhibits either pathogenic or protective roles depending on the disease stage and the background immune context [29–32]. In viral models using the neurovirulent MHV-JHM strain of murine β-coronavirus, NOS2 acts as a primary mediator of immune cell trafficking and acute inflammatory pathology [33]. However, Chen and Lane observed that NOS2-/- mice exhibited reduced neuronal apoptosis and mortality without alterations in demyelination severity [34] , whereas Perlman and colleagues reported that MHV-JHM-induced demyelination and spinal cord inflammation occur completely independently of NOS2 [35] . These conflicting observations highlight that the NOS2 function is highly dependent on viral strain, disease phase, and the surrounding immune landscape. Crucially, the specific role of NOS2 during the late remyelination phase (beyond day 30 p.i.) remains largely uncharacterized.

To address this gap, our laboratory utilizes the neurotropic MHV-RSA59 strain, a spike-gene recombinant murine β-coronavirus that induces a biphasic pathology mimicking key features of MS: an acute neuroinflammatory phase (days 5–7 p.i.) followed by chronic demyelination (day 30 p.i.)[36,37] . We previously demonstrated that NOS2-/- mice display accelerated early demyelination during the acute-to-adaptive transition (days 9–10 p.i.) and aggravated white matter destruction at day 30 p.i. compared to WT controls[38]. While these findings established a protective role for NOS2 against initial myelin damage, the necessity of NOS2 during the long-term regenerative phase (day 30 to day 60 p.i.) remained unknown.

In this study, we tested the hypothesis that NOS2 is required to orchestrate myeloid cell functional resolution, thereby permitting oligodendrocyte lineage progression and spontaneous

remyelination. We observed that WT mice exhibited substantial myelin recovery, whereas NOS2-/- mice did not achieve the same extent of myelin recovery compared to WT mice at day 60 p.i. By comparing wild-type and NOS2-/- mice at day 60 p.i., this research provides the first longitudinal evidence that NOS2 deficiency influences oligodendrocyte lineage progression. Our findings reveal that prolonged activation of CNS-resident microglia and infiltrating myeloid cells leads to a slower transition from a damage-associated to a regenerative state in the CNS of NOS2-/- mice compared with WT mice. Moreover, the persistent phagocytic activity of myeloid cells in the CNS of NOS2-/- mice, as observed in our current data, provides new insight into our previous understanding. In the absence of NOS2-mediated regulatory signals, myeloid cells remain activated and phagocytic, contributing to aggravated myelin loss and influencing the slower repair capacity of the oligodendrocyte lineage. Together, our results identify NOS2 as an essential molecular mediator that regulates myeloid cell functional states to foster CNS myelin repair.

Materials and Methods-

Animal ethics and transfer statement: In strict compliance with the guidelines of the Committee for Control and Supervision of Experiments on Animals (CCSEA), India, the Institutional Animal Ethics Committee (IAEC) of the Indian Institute of Science Education and Research (IISER) Kolkata examined and approved all animal experimental protocols and breeding practices. Dr. Bhaskar Saha of the National Center for Cell Science (NCCS), Pune, kindly provided the NOS2-/- mouse strain on a C57BL/6 genetic background. In conformity with CCSEA standards, an established Memorandum of Understanding (MOU) and authorized institutional transfer processes were followed during the transfer of these mice to the IISER Kolkata animal facility.

The NOS2-/- colony was bred, housed, and maintained at the IISER Kolkata animal facility under specific-pathogen-free (MHV-free) conditions with a regulated temperature and a 12-hour light/dark cycle, alongside wild-type (WT) C57BL/6 controls. To guarantee the genetic stability and purity of the knockout colony, genotyping was carried out regularly. Male mice aged five weeks and newborn pups were utilized as experimental cohorts. To reduce pain and discomfort, RSA59 intracranial inoculations and transcardial perfusions were carried out under proper anesthesia. Humane endpoints were carefully enforced for mice showing extreme distress before the planned sacrifice at day 30 or day 60 p.i. Body weight and clinical

neurological symptoms of the animals were monitored every day. The protocols IISERK/IAEC/AP/2024/125 and IISERK/IAEC/AP/2019/45 were utilized.

Inoculating mice with Virus

RSA59, an isogenic recombinant strain of the demyelinating mouse hepatitis virus, MHV A59 [39] , was administered intracranially to age-matched (5-week-old), MHV-free C57BL/6 male mice and NOS2-/- male mice on a C57BL/6 genetic background at 10,000 PFU (half of the 50% lethal dose is 20,000 PFU). Mock mice of both strains were injected with phosphate-buffered saline (PBS) plus 0.75% bovine serum albumin (BSA). Wild-type C57BL/6 mice (Jackson Laboratory, B6.129P2 tm1Lau/J and NOS2-/- mice[40] (Jackson Laboratory, B6.129P2-tm1Lau/J, Stock No. 002609) do not have any inherent pathological changes. Infected mice were monitored daily to assess changes in weight and disease symptoms. Progression of disease pathology in 5 week old C57BL/6 and NOS2-/- mice after RSA59-infection were documented regularly using a following scale 0: no disease symptoms; 0.5 represents ruffled fur; 1 represents a hunched back with mild ataxia; 1.5 represents a hunched back with mild ataxia and weakness in the hind limbs; 2 represents ataxia, balance issues, and/or partial paralysis; 2.5: one leg is totally paralyzed, has trouble moving, but can still move around with difficulty; 3: significantly reduced movement and extreme hunching, wasting, or paralysis of both hind limbs; 3.5: moribund, total paralysis, and extreme distress; 4: dead. Infected mice of both strains were sacrificed on day 30 p.i. (chronic phase) and on day 60 p.i. (post-chronic phase) for histopathological and immunohistochemical analyses, immunoblotting, immunofluorescence assays, and flow cytometry experiments.

Histopathology and immunohistochemical analysis

Tissues were harvested following transcardial perfusion with PBS and post-fixation with 4% paraformaldehyde for 36–48 hours. After that, those tissues were processed in gradually increasing concentrations of ethyl alcohol, xylene, and paraffin wax. Then, those processed tissues were embedded in a single mould using paraffin. Now, those embedded tissues were sectioned into Spinal cord transverse sections and mid-sagittal sections of the brain with a thickness of 5 µm using the Thermo Scientific HM 355 S sectioning system. Transverse sections of the spinal cord were stained with Luxol fast blue (LFB) stain to assess the demyelinated area in the spinal cord section, as described previously[41].

Immunohistochemical staining was conducted on brain and spinal cord sections using Ionized calcium-binding adaptor molecule 1 (Iba1) antibody (Wako; Catalog No. 019–19,741) in a 1:500 dilution. Primary antibodies were identified using an avidin–biotin immunoperoxidase technique (Vector Laboratories) with 3,3-diaminobenzidine (DAB) as the substrate[42]. Thereafter, all the slides were coded and analysed in a blinded manner.

Quantification of histopathological sections

Image analysis was performed using basic densitometric thresholding in Fiji (ImageJ, NIH Image, Scion Image), as described previously[43]. Briefly, Iba1-stained spinal cord and brain sections were imaged at 4X and 10X, respectively, so that the entire section (i.e., scan area) can be visualized within a single frame. To isolate and remove DAB-specific staining from the background hematoxylin staining, the RGB image was deconvolved into its three distinct colour channels. The perimeter of each brain and spinal cord section was digitally drawn, and the calculated area was expressed in square micrometers. A threshold value was set for each image to ensure that all $Iba1^+$cells were included. The amount of $Iba1^+$ staining for the brain and spinal cord section was expressed as the "% of $Iba1^+$ area."

LFB-stained transverse spinal cord sections from each mouse were analysed using Fiji (ImageJ, NIH Image, and Scion Image) to demarcate the demyelinated area [43,44]. The total perimeter of the white matter regions in each transverse section of the spinal cord was outlined, and the total area was calculated. Also, the total area of demyelinated regions was measured and compiled separately for each section. The percentage of demyelinated area per section per mouse was calculated.

Immunofluorescence assay on paraffin-embedded tissue sections

Infected mice were sacrificed at day 30 p.i. and day 60 p.i. Then, brain and spinal cord tissue sections were harvested, processed, and embedded in paraffin using the same steps as for histopathology and immunohistochemical analysis. After that, an immunofluorescence assay was conducted on the 5 µm-thick transverse sections of the spinal cord and mid-sagittal sections of the brain, as described previously[45]. Briefly, the slides containing spinal cord and brain sections were deparaffinized, then rehydrated and antigen-unmasked. Following a 15-minute incubation period at room temperature (RT), the slides were permeabilized using 0.2% Triton X-100 in PBS. Then the slides were incubated with 0.1 M glycine in PBS for 30 minutes and with 1mg/ml $NaBH_4$ in PBS for 5 minutes at RT /37 °C. These slides were then blocked for one hour at 37°C using 1% bovine serum albumin (BSA) prepared in 0.2% Triton X-100

in PBS. After that, primary antibodies made in blocking solution were incubated at 4°C for 16 hours. Each sample slide's sections were stained independently for the following: (i) anti-PLP home-made serum antibody (1:1), (ii) anti-MBP home-made serum antibody (1:1), (iii) anti-CC1(1:200, Merck, catalogue no. OP80) (iv) anti-A2B5 home-made serum antibody (1:10). Slides were then washed with 1X PBS solution and incubated with secondary antibodies AlexaFluor568 and AlexaFluor488 prepared in blocking solution in 1:1000 dilution for 1 hour at 37 °C. Lastly, the slides were washed again in 1X PBS and mounted with Vectashield containing DAPI to stain the nucleus.

Epifluorescence images were acquired using an Olympus IX-83 microscope and processed using Fiji-ImageJ software. Mean fluorescence intensity (MFI) of MBP- and PLP-stained spinal cord sections was measured, and $CC1^+$ and $A2B5^+$ cells per square millimetre were counted in each section of spinal cord, focusing mostly on the demyelinated area for day 30 p.i. and both demyelinated and intact white matter areas for day 60 p.i. using Fiji-ImageJ software.

Protein isolation and immunoblot analysis

Infected mice were euthanized following transcardial perfusion with 1X PBS, and an average of 150mg of whole brain tissue was flash-frozen in liquid nitrogen. The tissue was then lysed in 1 mL of RIPA buffer (0.1% SDS and 0.1% Triton X-100) containing 1X complete mini protease inhibitor cocktail tablets (#11836153001; Roche) and a phosphatase inhibitor cocktail containing 10 mM sodium orthovanadate, 10 mM sodium fluoride, and 10 mM sodium pyrophosphate. Brain tissues were mechanically homogenized through trituration and again disrupted by sonication. Then, those homogenates were centrifuged at 13,500 RPM for 30 minutes at 4°C. Afterward, the supernatant was carefully collected as a whole-protein extract. The BCA protein assay kit (Thermo Scientific, Rockford, IL, USA) was used to detect protein concentration. SDS-PAGE was used to separate an equivalent amount of protein, which was subsequently transferred to a polyvinylidene difluoride (PVDF) membrane. (Millipore, MA, USA). A transfer buffer containing 192 mM glycine, 25 mM Tris, and 20% methanol was used. 5% skim milk solution was prepared in TBS-T (Tris-buffered saline with 0.1% Tween-20) to block the PVDF membrane for 1 hour at room temperature. The membrane was then treated overnight at 4°C with the corresponding primary antibodies (Table 1) made in blocking solution. Following that, TBS-T was used to wash the primary antibody-bound membrane three times for ten minutes each. It was incubated with HRP-conjugated secondary IgG for one hour

at room temperature following the three washes. Lastly, immunoreactive bands were visualized using the SuperSignal West Pico PLUS Chemiluminescent Substrate (Thermo Scientific, MA, USA) according to the manufacturer's instructions, after three 10-minute washes with TBS-T. Images of the blots were captured using GENESys software (Genesys, Cambridge, UK) on a Syngene G: Box ChemiDoc system. Densitometric analysis of the bands from the blots was performed using ImageJ software [46,47] .

Flow cytometry analysis

Brain and spinal cord tissue from infected mice were harvested in 2 ml of RPMI containing 25 mM HEPES (pH 7.2) after transcardial perfusion with 20 ml PBS at days 30 and 60 p.i. Then, the harvested tissues were homogenized using a Tenbroeck tissue homogenizer. After the centrifugation of the tissue-homogenates at 450 × g for 10 minutes, cell pellets were resuspended in RPMI containing 25 mM HEPES, adjusted to 30% Percoll (Sigma-Aldrich, MO, USA), and underlaid with 1 ml of 70% Percoll. Then, a second centrifugation was performed at 800 g for 30 minutes at 4 °C, and the cells were recovered from the 30–70% interface, washed with RPMI, and suspended in FACS buffer (0.5% bovine serum albumin in Dulbecco's PBS). Specific cell types in the brain and spinal cord of infected mice were determined by staining with fluorochromes like Peridinin chlorophyll protein-Cyanine 5.5 (PerCP-Cy5.5), allophycocyanin (APC), and Brilliant Violet 421 (BV421) conjugated MAb for 45 minutes at 4°C in FACS buffer. Expression of surface markers was assessed using MAbs (all from BD Biosciences, as indicated in Table 1) specific for CD45 (clone Ly-5), CD11b (clone M1/70). Intranuclear staining for CD68 was performed after fixation and permeabilization (BD 562574) as per the manufacturer's guidelines.

A BD LSR Fortessa X-20 flow cytometer (BD Biosciences, CA, USA) was used to collect the samples, and FlowJo 10 software (Treestar, Inc., Ashland, OR) was used for analysis.[48]. Firstly, the cells were gated using forward scatter (FSC) and side scatter (SSC) to obtain a live-cell population. Then, FSC-A and FSC-W were used to determine the singlet population. Myeloid cells were gated from a primary gate on CD45. Single colours were used in all the experiments. Beads were gated based on their FSC/SSC pattern.

Statistical analyses

Values were expressed as mean values ± standard errors of the mean (SEM). Values were subjected to unpaired Student's t-tests with Welch's correction or ordinary one-way ANOVA with multiple comparison tests to calculate the significance of differences between the means.

GraphPad Prism 8 software (La Jolla, CA) was used for all statistical analyses. A statistically significant P-value was defined as less than 0. 05.

TABLE 1 Primary antibodies used in this study:

No.	Primary antibody	Application	Dilution	Source
1.	Anti-Iba1 (polyclonal)	IHC	1:500	Wako, Osaka, Japan
2.	Anti-CC1 (monoclonal)	IF	1:250	Merck, Darmstadt, Germany
3.	Anti-MBP	IF	1:1	Home-made serum antibody
4.	Anti-PLP	IF	1:1	Home-made serum antibody
5.	Anti-A2B5	IF	1:10	Home-made serum antibody
6.	Anti-PDGFR (polyclonal)	WB	1:1000	CST, MA, USA
7.	Anti-CNPase (Monoclonal)	WB	1:500	Sigma, MO, USA
8.	Anti-MBP	WB	1:10	Home-made serum antibody
9.	Beta-actin (Monoclonal)	WB	1:10000	Invitrogen, MA, USA
10.	Anti-CD45	Flow Cytometry	1:650	BD Bioscience, CA, USA
11.	Anti-CD11b	Flow Cytometry	1:650	BD Bioscience, CA, USA
12.	Anti-CD68	Flow Cytometry	1:650	BD Bioscience, CA, USA

- MBP, PLP, and A2B5- kind gift from Dr. Judith Grinspan, Children's Hospital of Philadelphia (CHOP), Philadelphia, USA

TABLE 2 Secondary antibodies used in this study:

No.	Secondary antibody	Application	Dilution	Source
1.	Alexa Fluor 488 Goat Anti-Mouse	IF	1:1000	Invitrogen, MA, USA
2.	Alexa Fluor 568 Donkey Anti-Mouse	IF	1:1000	Invitrogen, MA, USA
3.	Alexa Fluor 568 Donkey Anti-Rat	IF	1:1000	Invitrogen, MA, USA
4.	HRP-conjugated Rabbit secondary antibody	WB	1:10000	Invitrogen, MA, USA
5.	HRP-conjugated Rat secondary antibody	WB	1:10000	Invitrogen, MA, USA
6.	HRP-conjugated Mouse secondary antibody	WB	1:10000	Invitrogen, MA, USA

Results:

NOS2 deficiency leads to severe demyelination at day 30 post-infection (p.i.) and is associated with diminished myelin restoration at day 60 post-infection

Previously, our laboratory established that NOS2-/- mice exhibited early demyelination by day 9/10 p.i. and aggravated demyelination by day 30 p.i. [38]. Next, we aimed to determine whether this exacerbated disease pathology persists beyond the peak demyelination phase. Thus, we assessed myelin restoration in WT and NOS2-/- mice on day 60 p.i. Moreover, we examined temporal changes in myelin restoration between the two strains after day 30 p.i.

We observed significantly more demyelinating plaques in the spinal cord sections of NOS2-/- mice than in WT mice at day 30 p.i. (Fig. 1A, B, E). By day 60 p.i., significantly reduced demyelinating plaques were detected in the spinal cord of both strains (Fig. 1G). Although myelin restoration is observed in both strains by day 60 p.i., NOS2-/- mice exhibit substantially more demyelinating plaques in the spinal cord than WT mice at day 60 p.i. (Fig. 1C, D, F), suggesting a delayed myelin restoration process in the absence of NOS2.

These results imply that myelin restoration is evident in WT and NOS2-/- mice by day 60 p.i. However, myelin was mostly restored in WT mice, whereas NOS2-/- mice had still not achieved a similar extent of myelin restoration compared to WT mice at this reparative phase.

Absence of NOS2 results in the reduction of myelin basic protein (MBP) and proteolipid (PLP) expression in the spinal cord of both demyelination and remyelination phases

MBP and PLP are the two major myelin-forming proteins, and mature oligodendrocytes express these two proteins during their last stage of differentiation[49,50]. So, we next analysed the expression of MBP and PLP proteins in the myelin sheath to corroborate the evident differences in myelin sheath between WT and NOS2-/- mice at both the demyelination and remyelination phases.

Immunofluorescence was performed on the paraffin-embedded spinal cord sections of RSA59-infected NOS2-/- and WT mice using anti-MBP and anti-PLP antibodies. Immunofluorescence analysis using anti-MBP antibody revealed that RSA59-infected NOS2-/- mice exhibit a lower mean fluorescence intensity (MFI) of MBP protein in the spinal cord at day 30 p.i. in comparison to WT mice (Fig. 2A, B, C). A significant upregulation of MFI of MBP protein in the RSA59-infected spinal cord was observed in both strains at day 60 p.i. relative to day 30 p.i. (Fig. 2M). However, a strain-wise comparison revealed a significant downregulation of

MFI of MBP protein in the RSA59-infected spinal cord of NOS2-/- mice compared to WT mice at day 60 p.i. (Fig. 2D, E, F). Immunofluorescence analysis with an anti-PLP antibody showed that the MFI of PLP protein also followed a pattern similar to that of MBP protein (Fig. 2G-L,2N).

Collectively, these findings align with the apparent difference in myelin sheath that we observed between the two strains at both the myelin-loss and recovery phases.

NOS2 deficiency leads to downregulation of myelin basic protein (MBP) and proteolipid protein (PLP) expression in the brain tissue sample of both the demyelination and remyelination phases

We further determined whether the variations in myelin-forming protein expression identified in the spinal cord are also present in the brain[51]. Therefore, we analysed MBP and PLP expression in brain tissues to assess the effects of NOS2 deficiency on myelin integrity throughout the CNS.

We assessed MBP protein expression in brain tissue samples from both strains at both day-points by immunoblotting. At day 30 p.i., we observed a significant reduction in MBP protein expression in RSA59-infected brain samples from NOS2-/- mice compared with WT mice (Fig. 3I, J). By day 60 p.i. compared to day 30 p.i., the level of MBP expression increased significantly in the infected NOS2-/- mice, and in the infected WT mice, there was a trend of upregulation in the expression of MBP protein, though non-significant (Fig. 3M). However, a comparison between the two strains showed a significant downregulation of MBP protein in RSA59-infected brain samples from NOS2-/- mice compared to WT mice at day 60 p.i. (Fig. 3K, L). Then, we performed immunofluorescence on the paraffin-embedded brain sections of RSA59-infected NOS2-/- and WT mice using anti-MBP and anti-PLP antibodies. Representative immunofluorescence images were captured from the corpus callosum region of the paraffin-embedded brain sections across both stains at both day-points. The MBP expression pattern was consistent with the results obtained from immunoblotting analysis (Fig. 3A-D). Similarly, Representative immunofluorescence images from the corpus callosum region of brain sections revealed that PLP expression followed a pattern similar to MBP across both strains at days 30 and 60 p.i. (Fig. 3E-H).

Cumulatively, these observations are consistent with findings observed in the spinal cord, suggesting that NOS2 deficiency reduces the expression of MBP and PLP at both demyelination and remyelination phases across the CNS.

Absence of NOS2 causes a reduction in the number/expression of oligodendrocyte precursor cells (OPCs) and mature oligodendrocytes (OLs) in both the brain and spinal cord of RSA59-infected mice during the demyelination phase

Now, we examined the distribution of oligodendrocyte lineages across the CNS in NOS2-/- mice compared with WT mice at day 30 p.i. to identify the cause underlying the aggravated demyelination pathology. We used CC1 and CNPase antibodies to mark the mature oligodendrocyte (OL) pool and to determine the status of oligodendrocyte precursor cells (OPCs); we used A2B5 and PDGF-R antibodies [52,53].

NOS2-/- mice showed significantly reduced numbers of $CC1^+$ cells in the demyelinated region of the RSA59-infected spinal cord compared to WT mice at 30 p.i. (Fig. 4A-E). Also, the number of $A2B5^+$ cells was notably diminished in the demyelinated region of the spinal cord of NOS2-/- mice relative to WT mice at day 30 p.i. (Fig.4F-J). Similarly, representative immunofluorescence images of the corpus callosum regions of RfSA59-infected brain showed a reduction in the numbers of CC1+ and A2B5+ cells in the NOS2-/- mouse brains compared to WT mouse brains at the peak demyelination phase (Fig. 5A-D and Fig. 5G-J). Afterward, we quantitatively assessed the expression of another mature oligodendrocyte marker, CNPase, in protein samples from RSA59-infected brain tissues of NOS2-/- and WT mice by immunoblotting. We found a significant reduction in CNPase protein expression in the NOS2-/- brain compared with the WT brain (Fig. 5E, F). Likewise, for quantification, we examined the expression of another OPC marker, PDGF-R, using isolated brain protein and observed a trend toward reduced PDGF-R expression, though not significant, in the RSA59-infected NOS2-/- mice relative to WT mice during the demyelination phase (Fig. 5K, L).

Together, these results indicate that the lower abundance of oligodendrocyte lineage cells across the CNS of NOS2-/- mice relative to WT mice is associated with enhanced demyelination pathology and diminished expression of major myelin-forming proteins at day 30 p.i.

NOS2 deficiency is linked to a diminished number/expression of OPCs and a comparable number/expression of OL within both the spinal cord and the brain during the remyelination phase

After any demyelinating insult, OPCs proliferate and migrate to the lesion site, where they differentiate into myelinating oligodendrocytes that wrap their cytoplasmic processes around

denuded axons, forming a newly synthesized myelin sheath[54,55]. So, we assessed the status of oligodendrocyte lineages throughout the CNS in both NOS2-/- and WT mice at day 60 p.i.

NOS2-/- mice showed a notable decrease in the number of $A2B5^+$ cells in the demyelinated or intact white matter region of the RSA59-infected spinal cord compared to WT mice at 60 p.i. (Fig. 6F-J). Also, a non-significantly reduced number of $CC1^+$ cells was observed in the demyelinated or intact white matter region of the RSA59-infected spinal cord of NOS2-/- mice compared to WT mice at day 60 p.i. (Fig. 6A-E). Similarly, we found a reduced OPC pool and a slightly fewer OL cell population in the representative images of the corpus callosum region of paraffin-embedded brain sections from RSA59-infected NOS2-/- and WT mice, stained with anti-CC1 and anti-A2B5 antibodies (Fig. 7A-D and 7G-J). Furthermore, we quantitatively assessed the expression of CNPase and PDGF-R in protein lysates from the RSA59-infected brain tissues of NOS2-/- and WT mice at day 60 p.i. by immunoblotting. We found comparable CNPase expression in the infected brain samples from NOS2-/- and WT mice at day 60 p.i. (Fig. 7E, F). Also, we observed markedly reduced PDGF-R protein expression in brain samples from infected NOS2-/- mice compared with WT mice at day 60 p.i. (Fig. 7K, L).

Together, these findings suggest that differential distribution of oligodendrocyte lineages in NOS2-/- mice compared to WT mice may contribute to the reduced extent of myelin restoration observed during the remyelination phase.

Loss of NOS2 promotes increased activation of microglia/macrophages (MG/Mφ) and elevated accumulation of myeloid cell population in the CNS of RSA59-infected mice at the demyelination phase

A previous study from our lab established that activated MG/Mφ stripped myelin during a chronic demyelination state[36]. Also, it was shown earlier that NOS2-/- mice exhibited enhanced infiltration of the myeloid cell population compared to WT mice at day 9/10 p.i.[38]. So, we examined MG/Mφ activation and myeloid cell infiltration in the CNS of NOS2-/- mice compared with WT mice at day 30 p.i.

The activation of MG/Mφ was assessed by immunohistochemistry with an anti-Iba1 antibody. A significant increase in $Iba1^+$ MG/Mφ was observed in the RSA59-infected brain (Fig. 8A-E) and spinal cord (Fig. 9A-E) of NOS2-/- mice based on the quantification of staining intensity compared with WT mice at day 30 p.i. Moreover, we conducted flow cytometric analysis of

RSA59-infected whole brains and spinal cords from NOS2-/- and WT mice to quantify the absolute numbers of CNS-resident microglia and peripheral myeloid cell populations. Gating on $CD45^{hi}CD11b^{+}$ and $CD45^{lo}CD11b^{+}$ helps differentiate infiltrating peripheral myeloid cells from CNS-resident microglia after gating on live cells, followed by singlets. Then we analysed the number of $CD68^{+}$ cells (a phagocytic marker of infiltrating monocytes/macrophages and microglia) in the $CD45^{hi}CD11b^{+}$ and $CD45^{lo}CD11b^{+}$ cell populations. Flow cytometric analysis revealed a significant increase in the numbers of $CD45^{hi}CD11b^{+}$ expressing cells (Fig. 8F, G) and a trend of upregulation, though non-significant, in the numbers of $CD45^{lo}CD11b^{+}$ expressing cells (Fig. 8H, I) in the NOS2-/- brain compared to the WT brain at day 30 p.i. Also, we found a significantly higher number of CD68-expressing cells in the $CD45^{hi}CD11b^{+}$ and $CD45^{lo}CD11b^{+}$ cell populations in the NOS2-/- brain than in the WT brain at day 30 p.i. (Fig. 8J-M). Moreover, the flow cytometric results from the spinal cord were similar to those observed in the brain (Fig. 9F-M).

These observations indicate that phagocytic/activated myeloid cell populations are more abundant in the CNS of NOS2-/- mice than in WT mice at day 30 p.i. Also, enhanced infiltration of the myeloid cell population into the CNS of NOS2-/- mice was observed compared with WT mice during the chronic demyelination phase.

NOS2-/- deficiency leads to differential activation of CNS-resident microglia and infiltrated myeloid cell population in the brain and spinal cord during the remyelination phase

Sufficient clearance of myelin debris is necessary for remyelination to commence[56,57]. Phagocytic/activated MG and peripheral myeloid cells could facilitate myelin debris clearance after a demyelinating event, thereby promoting myelin recovery[58–60]. So, we further examined the numbers of phagocytic/activated MG and infiltrated myeloid cells in the CNS of RSA59-infected NOS2-/- mice relative to WT mice at day 60 p.i.

We analysed Iba1 staining intensity in brain sections from two strains at day 60 p.i. and observed increased $Iba1^{+}$ microglia/macrophage activation in the absence of NOS2 (Fig. 10A-E). In contrast to the brain, a comparable level of Iba1+ microglia/macrophage was found in the spinal cord of NOS2-/- mice compared to WT mice by day 60 p.i. (Fig. 11A-E). Furthermore, we quantified the absolute numbers of CNS-resident microglia and peripheral myeloid cells in RSA59-infected whole brains and spinal cords of NOS2-/- and WT mice via flow cytometric analysis. $CD45^{hi}CD11b^{+}$ and $CD45^{lo}CD11b^{+}$ gating were used to distinguish

the infiltrating myeloid cell population from the CNS-resident microglial population after gating on live cells, followed by singlets. Following the approach used during the demyelination phase, we next assessed the numbers of $CD68^+$ cells within the $CD45^{hi}CD11b^+$ and $CD45^{lo}CD11b^+$ cell populations of the brain and spinal cord across both strains at day 60 p.i. NOS2-/- mice showed enhanced numbers of $CD45^{hi}CD11b^+$ expressing cells (Fig.10F, G) along with a non-significant upward trend in the numbers of $CD45^{lo}CD11b^+$ expressing cells (Fig. 10H, I) in the NOS2-/- brain compared to the WT brain at day 60 p.i. In contrast, we observed an increased, though non-significant, number of $CD45^{hi}CD11b^+$ cells (Fig. 11F, G), which was associated with a non-significant downward trend in the $CD45^{lo}CD11b^+$ cell population (Fig. 11H, I) in the spinal cords of NOS2-/- mice relative to WT mice at day 60 p.i. Despite having a regional variation in the number of $CD45^{hi}CD11b^+$ and $CD45^{lo}CD11b^+$ expressing cells, NOS2-/- mice showed significantly increased numbers of $CD68^+$ cells among the $CD45^{hi}CD11b^+$ (Fig. 10J, L and 11J, L) and $CD45^{lo}CD11b^+$ (Fig. 10K, M and 11K, M) cell populations both in the brain and spinal cord compared to WT mice at day 60 p.i.

Accumulation of a markedly enhanced number of microglia and myeloid cells indicates that more myelin debris may persist across the CNS of NOS2-/- mice compared to WT mice during the remyelination phase.

Discussion:

This study resolves long-standing inconsistencies regarding the role of inducible nitric oxide synthase (NOS2) in coronavirus-induced demyelinating disease by establishing its indispensable requirement during late-stage central nervous system (CNS) remyelination. While previous investigations focused predominantly on early viral clearance and acute inflammatory tissue destruction, our 60-day longitudinal analysis uncovers a vital, protective role for NOS2 during the repair phase. Specifically, we demonstrate that NOS2 deficiency impairs the functional transition of CNS-resident microglia and infiltrating myeloid cells from a chronically activated, phagocytic phenotype into a pro-resolving, tissue-restorative state. This failure of myeloid resolution generates an inhibitory microenvironment that stalls oligodendrocyte progenitor cell (OPC) differentiation into mature, myelinating oligodendrocytes, thereby preventing spontaneous myelin restoration in NOS2-/- mice at day 60 p.i.

The literature surrounding the functional contribution of NOS2 to neuroinflammatory demyelination has historically been marked by conflicting conclusions across various animal models. Early studies utilizing the highly neurovirulent MHV-JHM strain suggested that NOS2 operated primarily as a mediator of acute mortality and apoptosis [34] or was entirely dispensable for inflammatory demyelination [35] . These discrepancies stem largely from fundamental differences in viral strain neurovirulence, host immune response kinetics, and, crucially, the experimental observational window evaluated. The MHV-JHM infection model causes rapid, severe acute mortality, restricting analytical evaluation strictly to early infection time points (days 7–14 post-infection). In contrast, the moderately neurovirulent MHV-RSA59 strain allows infected animals to survive the acute encephalitis phase. Thus, this model provides a robust and reliable platform to systematically investigate chronic demyelination at day 30 p.i. and subsequent endogenous remyelination at day 60 p.i.[36,37] . Extending our longitudinal observations out to day 60 post-infection reconciles these historical controversies, demonstrating that while acute NOS2 deficiency exacerbates initial myelin damage [38] . Its persistent absence impairs tissue recovery and prevents remyelination. Consequently, NOS2 is not merely a cytotoxic effector or passive bystander during neuroinflammation, but a critical regulatory checkpoint necessary for long-term tissue restoration.

The regulatory necessity of NOS2 observed in our viral model strongly parallels key insights derived from autoimmune models, particularly experimental autoimmune encephalomyelitis (EAE). In EAE, the role of NOS2 is similarly stage-dependent and complex [29–32] . While early paradigms classified NOS2-derived nitric oxide purely as a mediator of tissue damage, subsequent studies demonstrated that NOS2-/- mice often develop exacerbated, hyper-acute EAE marked by severe leukocyte infiltration and enhanced clinical disease severity [28,32] . Mechanistically, NOS2-derived nitric oxide serves as a crucial immunomodulatory brake in EAE, where it limits the expansion of autoreactive CD4+T cells, promotes apoptosis of encephalitogenic lymphocytes, and restrains pathogenic antigen-presenting cell activation[29,30] . Our findings in viral demyelination extend this immunomodulatory concept from peripheral immune priming to late-stage CNS-intrinsic tissue repair. Just as NOS2 restrains autoimmune hyper-reactivity in EAE, it acts in our viral model to terminate chronic microglial and macrophage activation. This convergence across autoimmune and viral models underscores that NOS2 functions as a fundamental regulatory checkpoint conserved across distinct neuroinflammatory etiologies to limit persistent tissue injury and permit CNS parenchymal recovery.

The human translational relevance of our findings is underscored by histopathological evidence from Multiple Sclerosis (MS) patients. In MS brain and spinal cord tissue, NOS2 expression and nitric oxide reactive byproducts, such as 3-nitrotyrosine, are markedly elevated within active and chronic active lesion borders, localized predominantly to reactive astrocytes, activated microglia, and infiltrating macrophages[25] . Historically, this elevated NOS2 expression was viewed as purely destructive, directly causing mitochondrial injury, axonal transection, and oligodendrocyte death. However, modern neuropathological studies of human MS lesions demonstrate that myeloid cells display highly dynamic, intermediate activation states that evolve across different lesion stages [25] . Our study bridges a critical translational gap by revealing that NOS2 is not solely a driver of damage in MS, but an active regulator required for tissue repair. By demonstrating that NOS2 signaling is necessary for myeloid cells to resolve their inflammatory profile and allow OPC maturation, our findings offer a compelling mechanistic explanation for why human MS lesions with persistent, unresolving myeloid activation frequently fail to remyelinate.

A pivotal finding of this study is that NOS2-/- mice display sustained, dysregulated activation and prolonged phagocytic activity in resident microglia and infiltrating macrophages at day 60 p.i. In wild-type mice, the resolution phase is characterized by a gradual attenuation of proinflammatory signaling, down-regulation of phagocytic activity, and a phenotypic shift in myeloid cells toward a pro-regenerative profile that supports repair. In NOS2-/- mice, however, myeloid cells remain trapped in a chronically activated, damage-associated state. Although nitric oxide is traditionally categorized as a cytotoxic gasomediator, accumulating evidence indicates that low-to-moderate physiological levels of NOS2-derived nitric oxide function as an essential negative feedback signal to limit NF-κβ activation, suppress excessive leukocyte infiltration, and regulate mitochondrial bioenergetics in myeloid populations [25,32] . In the absence of NOS2-derived signals, this intrinsic regulatory brake is lost, resulting in uninhibited myeloid activation. Unresolved phagocytosis and the continuous secretion of secondary inflammatory cytokines by NOS2-/- microglia and macrophages sustain a hostile, toxic microenvironment within demyelinated spinal cord white matter tracts.

Furthermore, this study establishes that persistent myeloid activation directly disrupts the delicate intercellular cross-talk required for oligodendrocyte lineage progression and repair. Endogenous remyelination relies on a tightly orchestrated sequence of events, including OPC proliferation, migration to demyelinated lesions, and subsequent differentiation into mature,

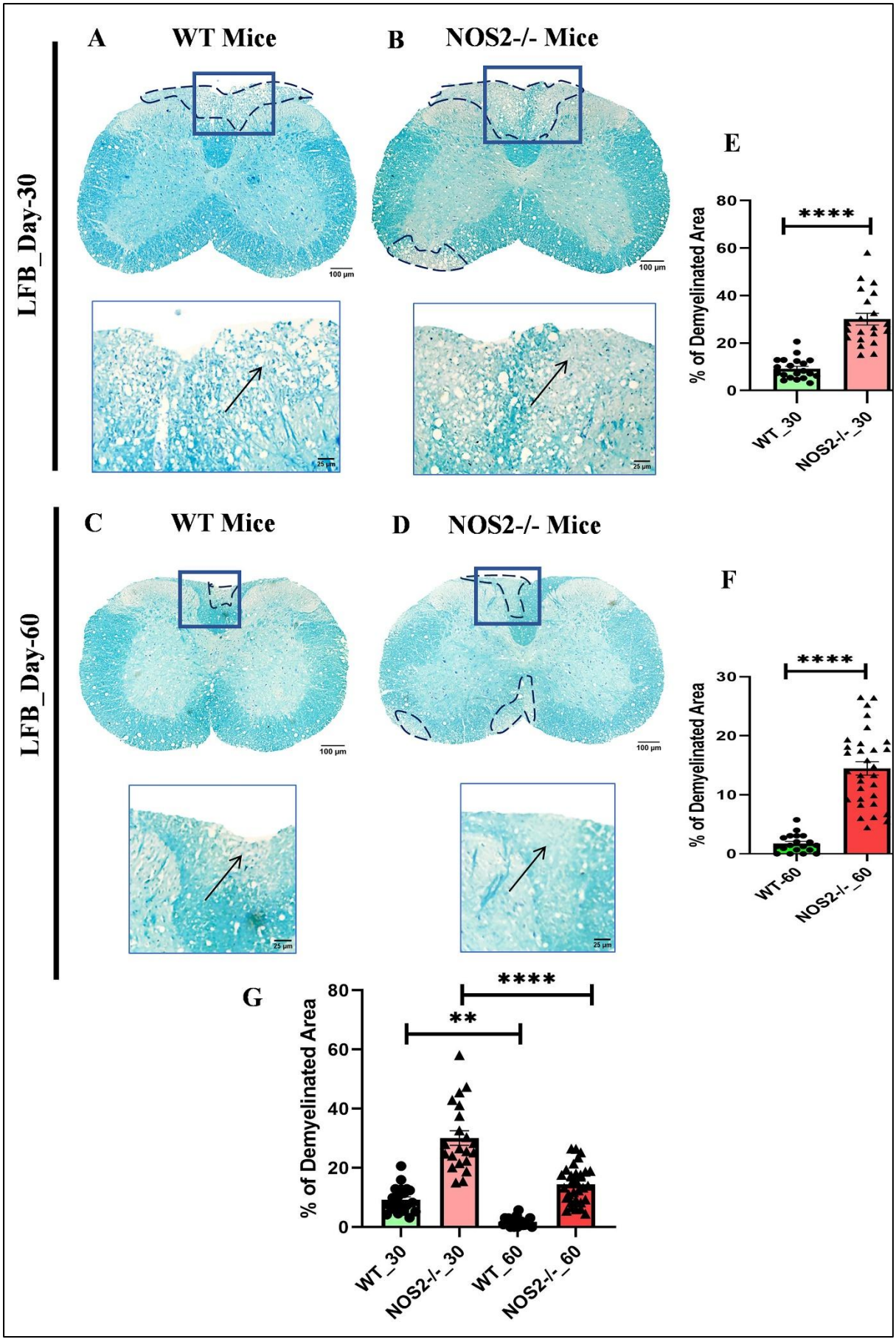
myelin-synthesizing oligodendrocytes expressing PLP and MBP [7,13] . Our quantitative characterization of the oligodendrocyte lineage reveals that oligodendrocyte precursor cells expressing A2B5 and PDGFRα are successfully recruited to lesion sites in both wild-type and NOS2-/- Mice, though the OPC pool is reduced in the CNS of NOS2-/- mice compared with WT mice at day 60 p.i. Also, their terminal maturation into functional, myelinating oligodendrocytes is slowed down in NOS2-/- mice at day 60 p.i. This differentiation delay may be linked with inefficient clearance of myelin debris by phagocytic microglia/macrophages. Functional OPC differentiation requires strict environmental cues, involving the timely phagocytic clearance of inhibitory myelin debris followed by a prompt cessation of proinflammatory cytokine release [20,22,56]. Chronic activation of NOS2-/- myeloid cells disrupts this temporal sequence. Unresolved immune activation and prolonged, dysregulated phagocytosis impair the key signaling pathways necessary for OPC terminal maturation. As a result, despite maintaining an adequate pool of progenitor cells, NOS2-/- mice fail to generate mature oligodendrocytes capable of synthesizing new myelin sheaths around denuded axons.

These findings hold direct translational significance for Multiple Sclerosis and post-viral neuroinflammatory conditions. Pan-NOS chemical inhibition has previously been proposed as a candidate therapeutic approach to mitigate oxidative stress and tissue injury in acute lesions. However, clinical trials and preclinical studies targeting NOS isoforms have produced inconsistent and often disappointing outcomes [25,28] . Our findings urge substantial caution regarding broad, unselective NOS2 blockade during chronic disease stages. Inhibiting NOS2 activity during tissue repair disrupts the endogenous regulatory signals required for inflammatory resolution and oligodendrocyte maturation, thereby preventing endogenous remyelination. Instead, future therapeutic strategies should aim to target downstream NOS2-regulated pathways to foster a pro-repair myeloid phenotype while avoiding cytotoxic oxidative damage.

Conclusion:

In conclusion, this study demonstrates that NOS2 is essential for endogenous remyelination and oligodendrocyte lineage progression following murine β-coronavirus-induced neuroinflammation. Beyond its established role in early viral control, NOS2 serves as a vital molecular switch that terminates chronic myeloid cell activation and phagocytic drive during the tissue recovery phase. In the absence of NOS2, persistent microglial and macrophage activation blocks OPC maturation into functional, myelinating oligodendrocytes, leading to

repair failure. Redefining NOS2 as an essential pro-regenerative mediator provides a novel conceptual framework for therapeutic interventions designed to promote central nervous system repair in Multiple Sclerosis and post-viral neuroinflammatory diseases.


A
WT Mice
B
NOS2-/- Mice
LFB_Day-30
100 µm
25 µm
E
% of Demyelinated Area
****
WT_30
NOS2-/-_30
C
WT Mice
D
NOS2-/- Mice
LFB_Day-60
F
WT-60
NOS2-/-_60
G
**
WT_30
NOS2-/-_30
WT_60
NOS2-/-_60

547

Figure 1. NOS2 deficiency exacerbates demyelination and subsequently delays myelin restoration: 5 µm thick transverse spinal cord sections of RSA59-infected (10,000 PFUs) WT and NOS2-/- mice were stained with Luxol fast blue (LFB) to check the demyelinating plaque both at days 30 and 60 p.i. (A) represents the spinal-cord section of WT mice, and (B) represents the spinal cord of NOS2-/- mice at day 30 p.i. (C) represents the spinal-cord section of WT mice, and (D) represents the spinal cord of NOS2-/- mice at day 60 p.i. Blue boxes indicate the demyelinated area below the corresponding spinal cord section. (E-G) represent the quantification graph of the percentage of demyelinating area between two strains at day 30 p.i. (E), at day 60 p.i. (F), and across both time points (G). Scale bar: 100 µm, 25 µm. Each group consists of 4–6 mice. Each dot in the graph represents a section from a single spinal cord, and 1 to 6 sections representing various spinal cord regions were studied. Mean ± SEM was used to express the findings. * $P < 0.05$ was regarded as significant; asterisks indicate statistical significance determined by the unpaired Student's t-test with Welch correction (where two groups were compared) and ordinary one-way ANOVA when more than two groups were compared. *$P < 0.05$, ***$P < 0.001$, ****$P < 0.0001$, ns-not significant.

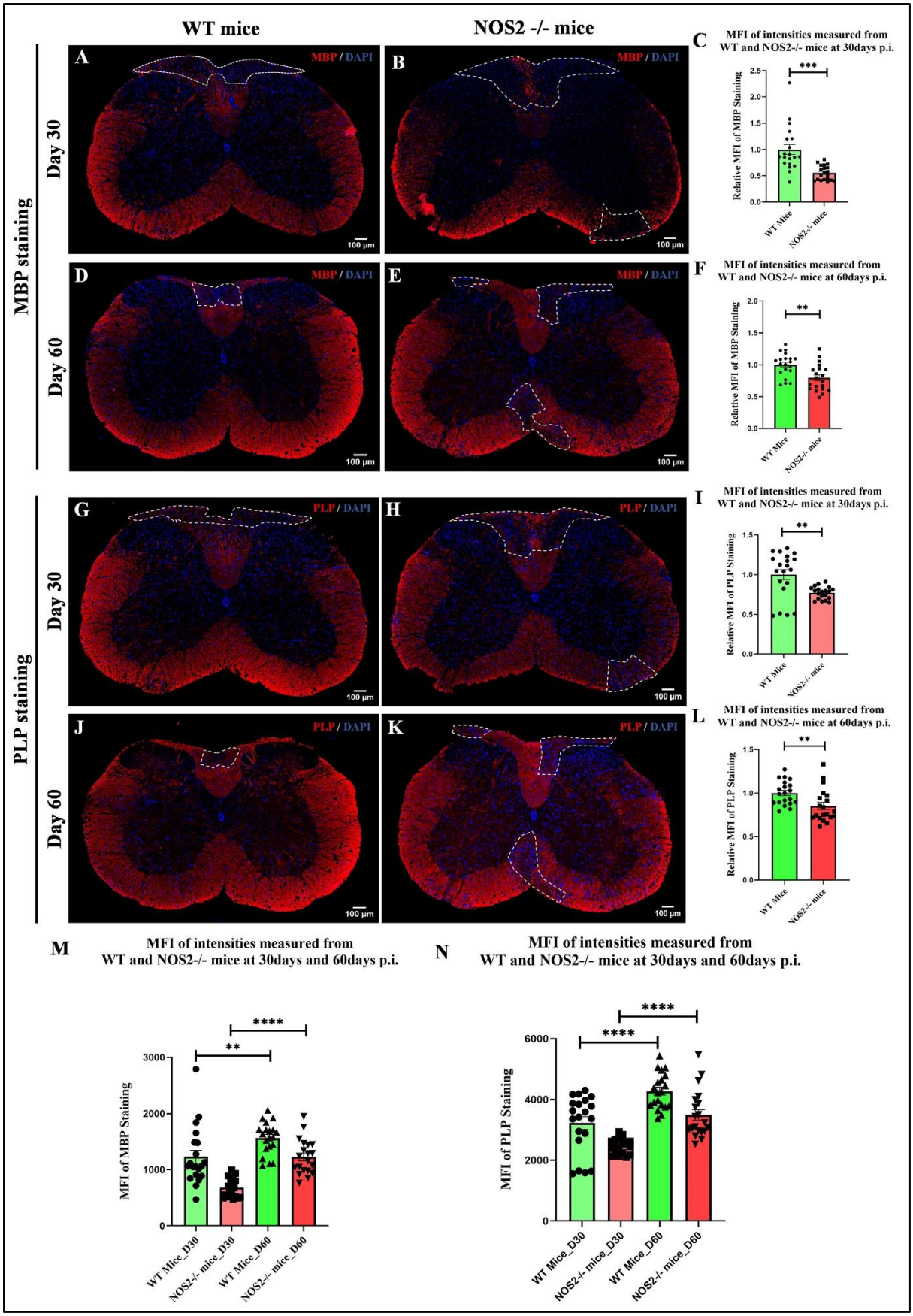
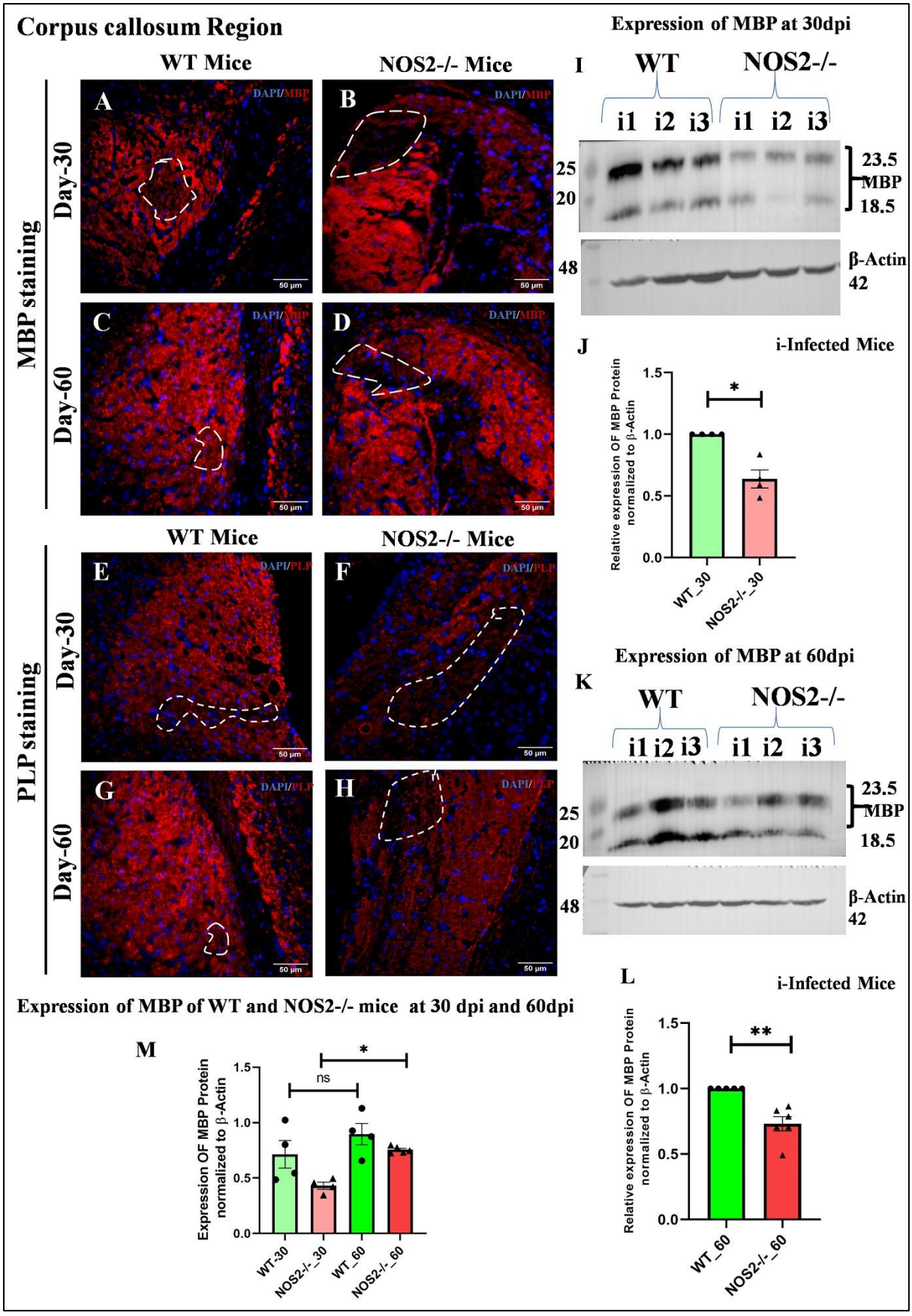
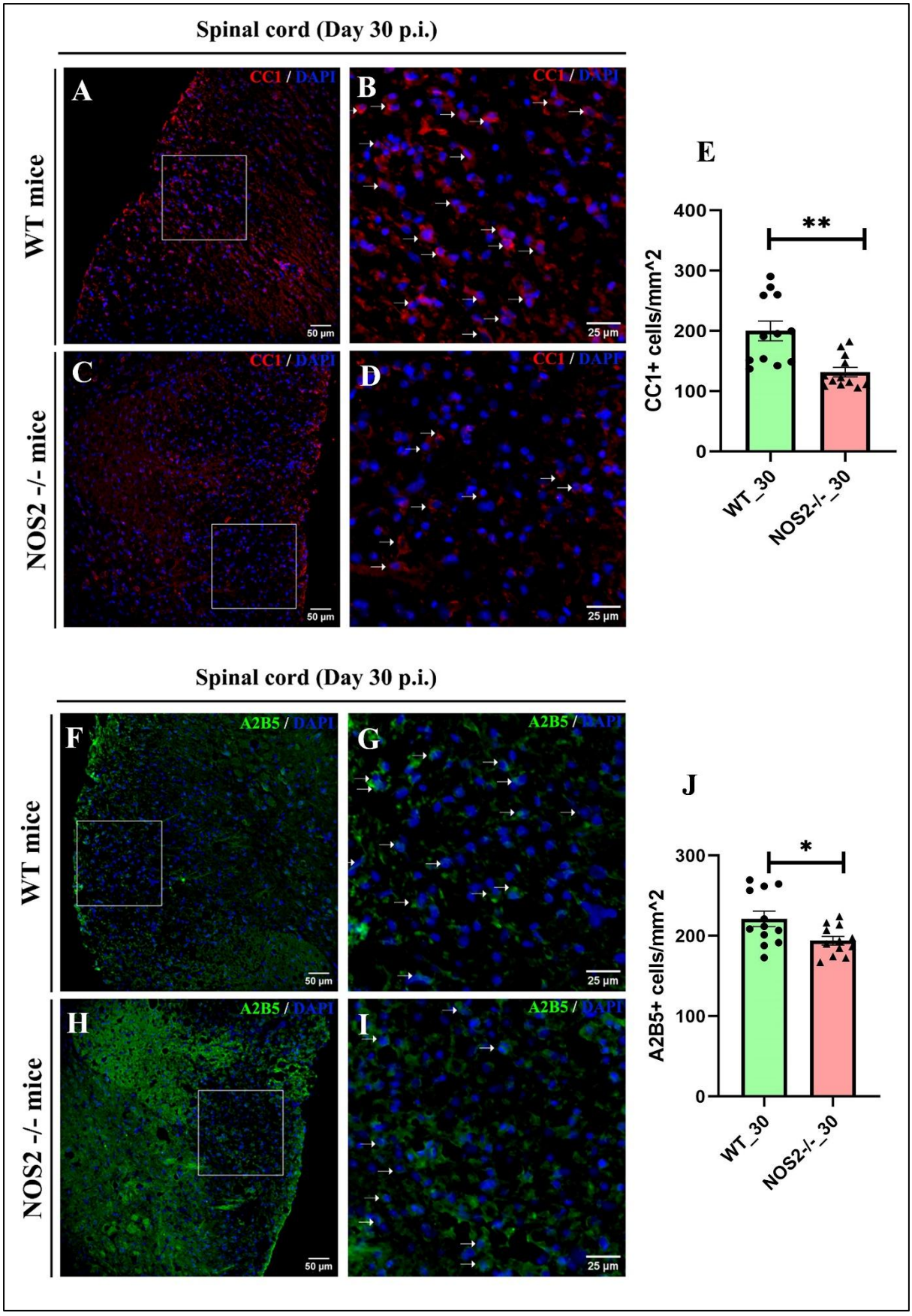

WT mice
NOS2 -/- mice
MBP staining
Day 30
Day 60
PLP staining
A
B
C
D
E
F
G
H
I
J
K
L
M
N
MBP / DAPI
PLP / DAPI
100 µm
MFI of intensities measured from WT and NOS2-/- mice at 30days p.i.
MFI of intensities measured from WT and NOS2-/- mice at 60days p.i.
Relative MFI of MBP Staining
Relative MFI of PLP Staining
WT Mice
NOS2-/- mice
MFI of intensities measured from WT and NOS2-/- mice at 30days and 60days p.i.
MFI of MBP Staining
MFI of PLP Staining
WT Mice_D30
NOS2-/- mice_D30
WT Mice_D60
NOS2-/- mice_D60

Figure 2. NOS2 deficiency results in reduced intensities of MBP and PLP in the spinal cord: 5 µm thick transverse spinal cord sections of RSA59-infected (10,000 PFUs) WT and NOS2-/- mice were immunostained with anti-MBP and anti-PLP antibodies, followed by epi-fluorescence microscopy. (A-B) represent the spinal cord sections of WT and NOS2-/- mice, respectively, stained with anti-MBP antibody at day 30 p.i. (C) represents the quantification graph of mean fluorescence intensity (MFI) of MBP measured at day 30 p.i. (D-E) represent the spinal cord sections of WT and NOS2-/- mice, respectively, stained with anti-MBP antibody at day 60 p.i. (F) represents the quantification graph of MFI of MBP measured at day 60 p.i. (G-H) represent the spinal cord sections of WT and NOS2-/- mice, respectively, stained with anti-PLP antibody at day 30 p.i. (I) represents the quantification graph of MFI of PLP measured at day 30 p.i. (J-K) represent the spinal cord sections of WT and NOS2-/- mice, respectively, stained with anti-PLP antibody at day 60 p.i. (L) represents the quantification graph of MFI of PLP measured at day 60 p.i. (M-N) represents the quantification graph of MFI for MBP and PLP, respectively, measured from WT and NOS2-/- mice at days 30 and 60 p.i. White dashed lines indicate demyelinated areas in spinal cord sections from both strains. Scale bar 100 µm. Each group has n = 4 mice. Each dot in the graph represents a section from a single spinal cord, and 1 to 5 sections representing various spinal cord regions were studied. Mean ± SEM was used to express the results. * $P < 0.05$ was regarded as significant; asterisks indicate statistical significance determined using the unpaired Student's t-test with Welch correction (where two groups were compared) and ordinary one-way ANOVA when more than two groups were compared. *$P < 0.05$, **$P < 0.01$, ***$P < 0.001$, ****$P < 0.0001$, and ns-not significant


Corpus callosum Region
WT Mice
NOS2-/- Mice
MBP staining
Day-30
Day-60
A
B
C
D
DAPI/MBP
50 µm
PLP staining
E
F
G
H
DAPI/PLP
Expression of MBP at 30dpi
I
WT
NOS2-/-
i1 i2 i3 i1 i2 i3
25
20
48
23.5
MBP
18.5
β-Actin
42
J
i-Infected Mice
Relative expression OF MBP Protein normalized to β-Actin
1.5
1.0
0.5
0.0
*
WT_30
NOS2-/-_30
Expression of MBP at 60dpi
K
L
i-Infected Mice
**
WT_60
NOS2-/-_60
Expression of MBP of WT and NOS2-/- mice at 30 dpi and 60dpi
M
Expression OF MBP Protein normalized to β-Actin
ns
*
WT-30
NOS2-/-_30
WT_60
NOS2-/-_60

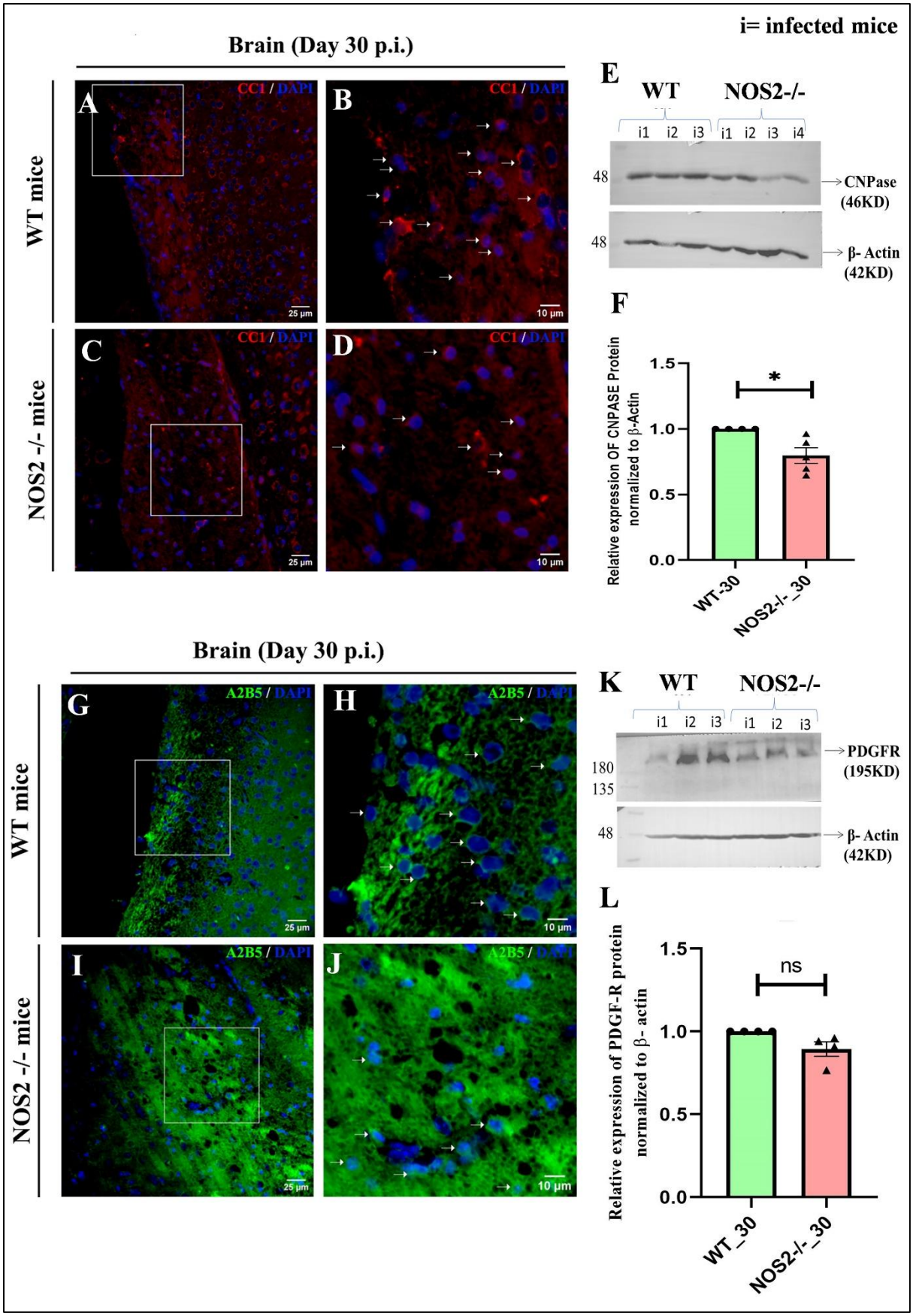
607

Figure 3. NOS2 deficiency leads to diminished expression of MBP and PLP in the brain: 5 μm thick mid-sagittal brain sections of RSA59-infected (10,000 PFUs) WT and NOS2-/- mice were immunostained with anti-MBP and anti-PLP antibodies, followed by epi-fluorescence microscopy. (A-B) represent the corpus callosum region of the brain section from WT and NOS2-/- mice, respectively, at day 30 p.i., where MBP is in red. (C-D) represent the corpus callosum region of the brain section from WT and NOS2-/- mice, respectively, at day 60 p.i., where MBP is in red. (E-F) represent the corpus callosum region of the brain section from WT and NOS2-/- mice, respectively, at day 30 p.i. , where PLP is in red. (G-H) represent the corpus callosum region of the brain section from WT and NOS2-/- mice, respectively, at day 60 p.i. , where PLP is in red. DAPI appears in blue across all immunofluorescence images. Scale bar: 50 μm. White-dashed lines indicate the demyelinated region of the corpus callosum, where the intensity of MBP and PLP is lower in both strains across both day points. (I and J) represent the corresponding immunoblot and quantification graphs of MBP protein in RSA59-infected WT and NOS2-/- mouse-brains at day 30 p.i. (K and L) represent the corresponding immunoblot and quantification graphs of MBP protein in RSA59-infected WT and NOS2-/- mouse-brains at day 60 p.i. (M) represents the quantification graph of MBP protein in RSA59-infected WT and NOS2-/- mouse-brains across both days post-infection. Mean ± SEM was used to express the results (n = 4-6 per group). * $P < 0.05$ was regarded as significant; asterisks indicate statistical significance determined using the unpaired Student's t-test with Welch correction (where two groups were compared, and ordinary one-way ANOVA when more than two groups were compared). *$P < 0.05$, **$P < 0.01$, ***$P < 0.001$, ****$P < 0.0001$, and ns-not significant


Spinal cord (Day 30 p.i.)
WT mice
NOS2 -/- mice
A
B
C
D
CC1 / DAPI
50 µm
25 µm
E
CC1+ cells/mm^2
400
300
200
100
0
**
WT_30
NOS2-/-_30
Spinal cord (Day 30 p.i.)
F
G
H
I
A2B5 / DAPI
J
A2B5+ cells/mm^2
*

638

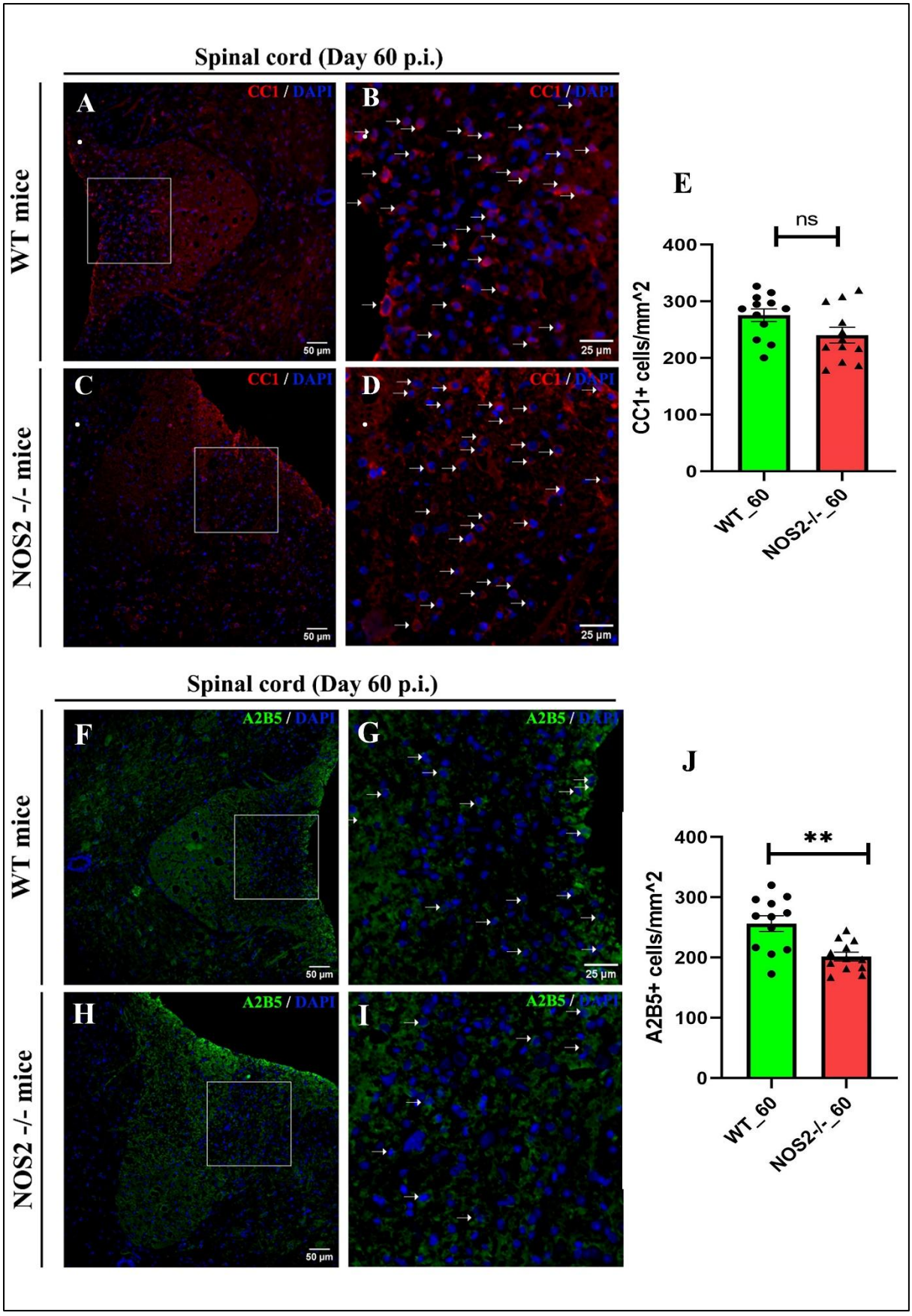
Figure 4. NOS2 deficiency leads to a reduced number of OPCs and OLs in the spinal cord: 5 µm thick transverse spinal cord sections of RSA59-infected (10,000 PFUs) WT and NOS2-/- mice were immunostained with anti-A2B5 and anti-CC1 antibodies, followed by epi-fluorescence microscopy at day 30 p.i. (A) represent a region of the spinal cord section from WT mice at day 30 p.i., where DAPI is in blue, and CC1 is in red. (C) represent a region of spinal-cord section from NOS2-/- mice at day 30 p.i., where DAPI is in blue and CC1is in red. (B-D) represent the white box in the region of the spinal cord of WT and NOS2-/- mice, respectively, with $CC1^+$ cells indicated by a white arrow. (E) Quantification graph of $CC1^+$ cells/mm^2 in RSA59-infected WT and NOS2-/- spinal cord at day 30 p.i. (F) represents a region of spinal cord section from WT mice at day 30 p.i., where DAPI is in blue, and A2B5 is in green. (H) represents a region of the spinal-cord section from NOS2-/- mice at day 30 p.i., where DAPI is in blue, and A2B5 is in green. (G-I) represent the white box in the region of the spinal cord of WT and NOS2-/- mice, respectively, where $A2B5^+$ cells are indicated by a white arrow. (J) Quantification graph of $A2B5^+$ cells/mm^2 in RSA59-infected WT and NOS2-/- spinal cord at day 30 p.i. 50 µm and 25 µm scale bars; n = 4 mice /group. Each dot in the graph represents one section from a single spinal cord, and one to three sections representing various spinal cord regions were analysed. Mean ± SEM was used to express the results. * Asterisks indicate statistical significance, which was determined using unpaired Student's t-test with Welch correction; $P < 0.05$ was regarded as significant. *$P < 0.05$, **$P < 0.01$, ***$P < 0.001$, ****$P < 0.0001$, ns-not significant.


i= infected mice
Brain (Day 30 p.i.)
WT mice
NOS2 -/- mice
A
B
C
D
CC1 / DAPI
25 µm
10 µm
E
WT
NOS2-/-
i1 i2 i3 i1 i2 i3 i4
48
CNPase
(46KD)
β- Actin
(42KD)
F
Relative expression OF CNPASE Protein
normalized to β-Actin
1.5
1.0
0.5
0.0
*
WT-30
NOS2-/- _30
Brain (Day 30 p.i.)
G
H
I
J
A2B5 / DAPI
K
WT
NOS2-/-
i1 i2 i3 i1 i2 i3
180
135
PDGFR
(195KD)
L
Relative expression of PDGF-R protein
normalized to β- actin
ns
WT _30
NOS2-/- _30

669

670

Figure 5. NOS2 deficiency leads to decreased number of OPCs and OLs in the brain: 5 µm-thick transverse spinal cord sections of RSA59-infected (10,000 PFUs) WT and NOS2-/- mice were immunostained with anti-A2B5 and anti-CC1 antibodies, followed by epi-fluorescence microscopy at day 30 p.i. (A) represents the corpus callosum region of the brain section from WT mice at day 30 p.i., where DAPI is in blue, and CC1 is in red. (C) represents the corpus callosum region of the brain section from NOS2-/- mice at day 30 p.i., where DAPI is in blue, and CC1 is in red. (B-D) represent the white box in the corpus callosum region of the brain section of WT and NOS2-/- mice, respectively, to indicate the $CC1^+$ cells with a white arrow. (G) represents the corpus callosum region of the brain section from WT mice at day 30 p.i., where DAPI is in blue, and A2B5 is in green. (I) represents the corpus callosum region of the brain section from NOS2-/- mice at day 30 p.i., where DAPI is in blue, and A2B5 is in green. (H-J) represent the white box in the corpus callosum region of the brain section of WT and NOS2-/- mice, respectively, indicating $A2B5^+$ cells with a white arrow. Scale bar 25 µm ,10 µm. (E and F) represent the corresponding immunoblot and quantification graph of CNPase protein in RSA59-infected WT and NOS2-/- mouse-brain at day 30 p.i. (K and L) represent the corresponding immunoblot and quantification graph of PDGF-R protein in RSA59-infected WT and NOS2-/- mouse brain at day 30 p.i. Mean ± SEM was used to express the findings (n = 4-5 per group). *P < 0.05 was regarded as significant; asterisks indicate statistical significance determined using the unpaired Student's t-test plus Welch correction. *P < 0.05, **P < 0.01, ***P < 0.001, ****P < 0.0001.


Spinal cord (Day 60 p.i.)
WT mice
NOS2 -/- mice
A
B
C
D
CC1 / DAPI
50 µm
25 µm
E
ns
CC1+ cells/mm^2
400
300
200
100
0
WT_60
NOS2-/-_60
Spinal cord (Day 60 p.i.)
F
G
H
I
A2B5 / DAPI
J
**
A2B5+ cells/mm^2

701

Figure-6. NOS2 deficiency leads to a differential distribution of OPCs and OLs in the spinal cord: 5 µm thick transverse spinal cord sections of RSA59-infected (10,000 PFUs) WT and NOS2-/- mice were immunostained with anti-A2B5 and anti-CC1 antibodies, followed by epi-fluorescence microscopy at day 60 p.i. (A) represents a region of the spinal cord section from WT mice at day 60 p.i., where DAPI is in blue, and CC1 is in red. (C) represents a region of spinal-cord section from NOS2-/- mice at day 60 p.i., where DAPI is in blue and CC1is in red. (B-D) represent the white box in the region of the spinal cord of WT and NOS2-/- mice, respectively, with $CC1^+$ cells indicated by a white arrow. (E) Quantification graph of $CC1^+$ cells/mm^2 in RSA59-infected WT and NOS2-/- spinal cord at day p.i. (F) represents a region of the spinal cord section from WT mice at day p.i., where DAPI is in blue, and A2B5 is in green. (H) represents a region of spinal-cord section from NOS2-/- mice at day 60 p.i., where DAPI is in blue, and A2B5 is in green. (G-I) represent the white box in the region of the spinal cord of WT and NOS2-/- mice, respectively, where $A2B5^+$ cells are indicated by a white arrow. (J) Quantification graph of $A2B5^+$ cells/mm^2 in RSA59-infected WT and NOS2-/- spinal cord at day 60 p.i. Scale bar 50 µm, 25 µm. n = 4 mice in each group. Each dot in the graph indicates one section from a single spinal cord, and one to three sections representing various spinal cord regions were studied. Mean ± SEM was used to express the results. * Asterisks indicate statistical significance, which was determined by unpaired Student's t-test with Welch correction; $P < 0.05$ was regarded as significant. *$P < 0.05$, **$P < 0.01$, ***$P < 0.001$, ****$P < 0.0001$, and ns-not significant.

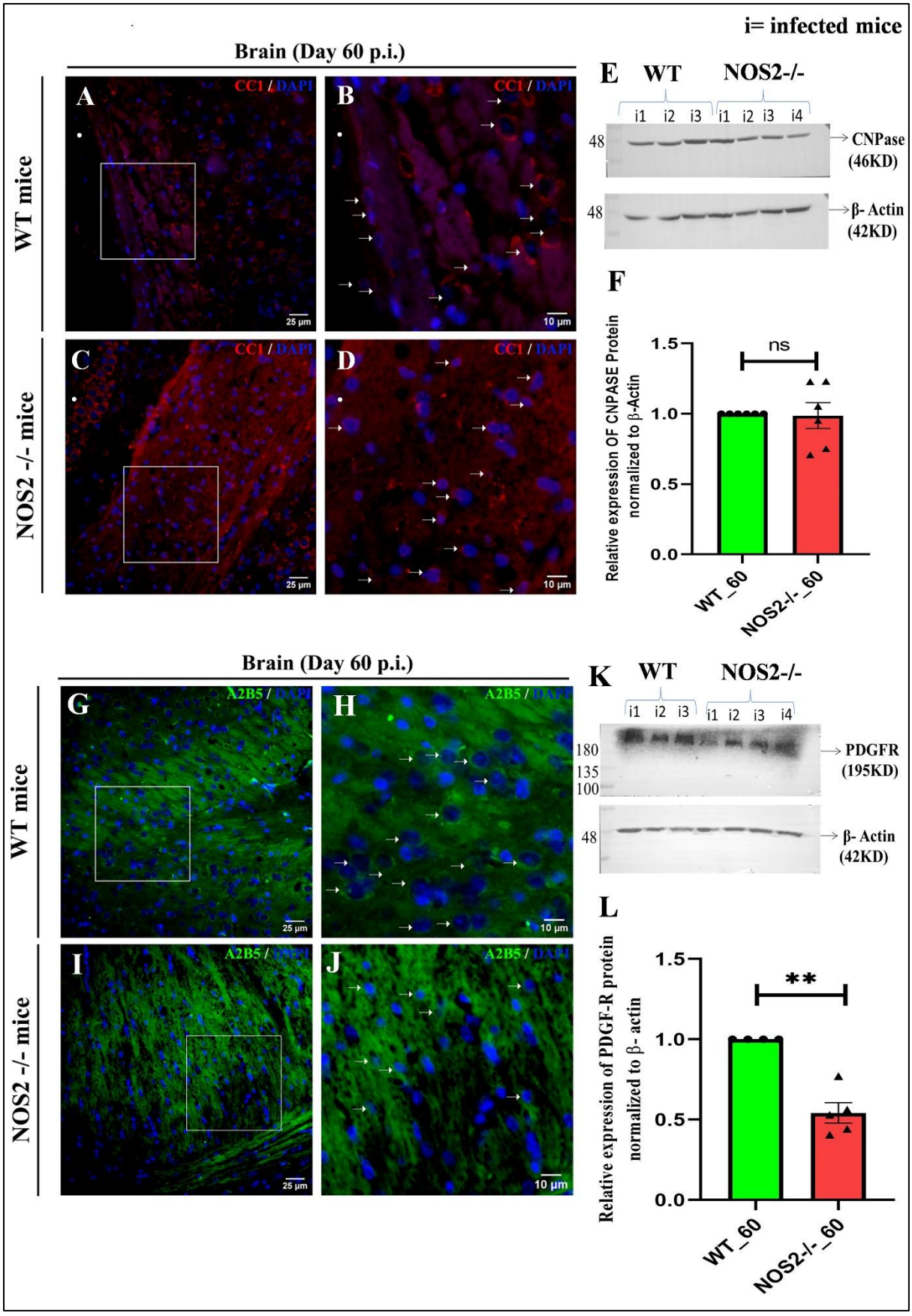
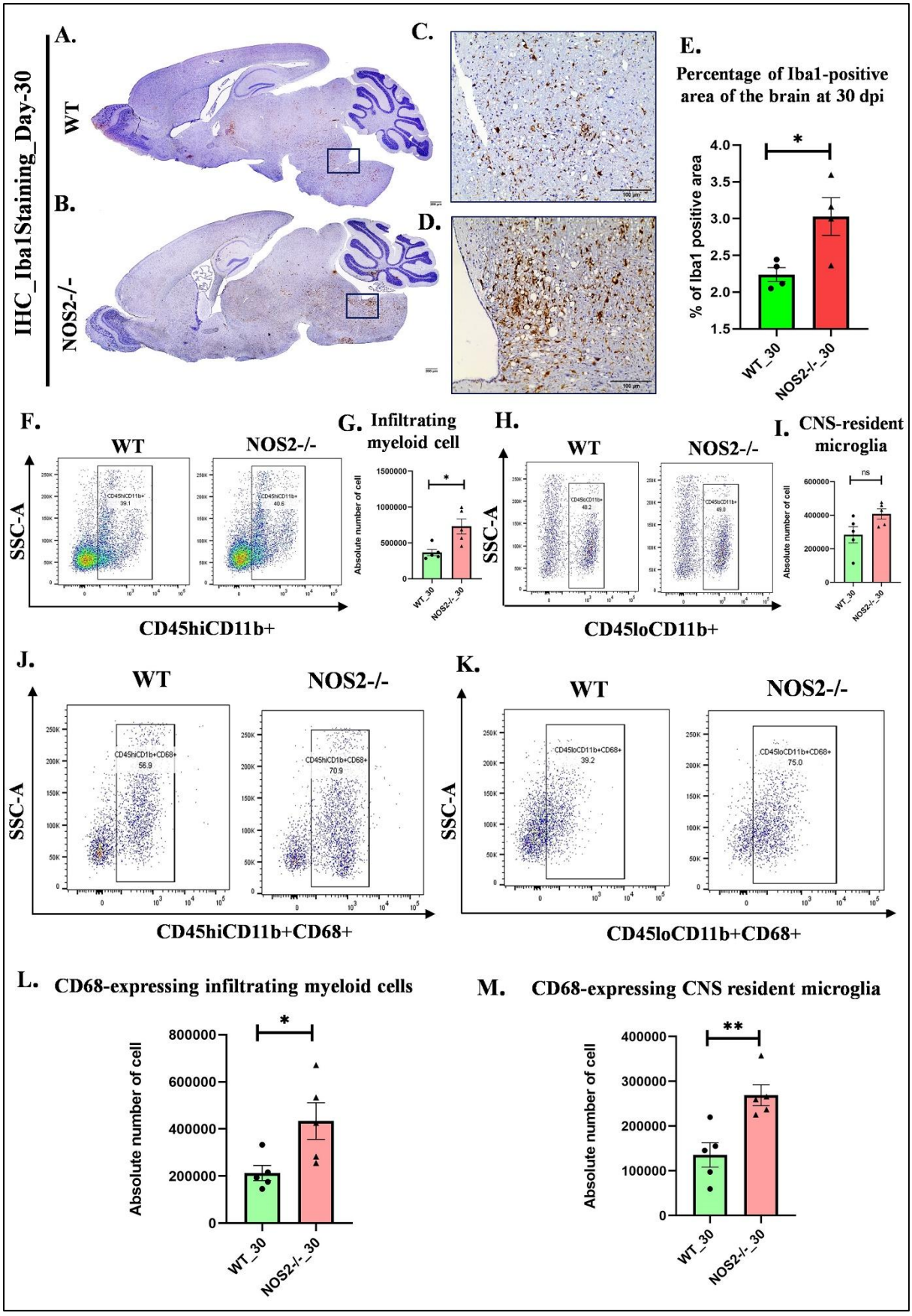

i= infected mice
Brain (Day 60 p.i.)
WT mice
NOS2 -/- mice
A
B
C
D
CC1 / DAPI
25 µm
10 µm
E
WT
NOS2-/-
i1 i2 i3 i1 i2 i3 i4
48
CNPase (46KD)
β- Actin (42KD)
F
Relative expression OF CNPASE Protein normalized to β-Actin
ns
1.5
1.0
0.5
0.0
WT _60
NOS2-/- _60
Brain (Day 60 p.i.)
G
H
I
J
A2B5 / DAPI
K
i1 i2 i3 i1 i2 i3 i4
180
135
100
PDGFR (195KD)
β- Actin (42KD)
L
Relative expression of PDGF-R protein normalized to β- actin
**

Figure-7. NOS2 deficiency leads to a differential distribution of OPCs and OLs in the brain: 5 µm thick mid-sagittal brain sections of RSA59-infected (10,000 PFUs) WT and NOS2-/- mice were immunostained with anti-A2B5 and anti-CC1 antibodies, followed by epi-fluorescence microscopy at day 60 p.i. (A) represents the corpus callosum region of the brain section from WT mice at day 60 post-infection, where DAPI is in blue, and CC1 is in red. (C) represents the corpus callosum region of the brain section from NOS2-/- mice at day 60 p.i., where DAPI is in blue, and CC1 is in red. (B-D) represent the white box in the corpus callosum region of the brain of WT and NOS2-/- mice, respectively, indicating the $CC1^+$ cells with a white arrow. (G) represents the corpus callosum region of the brain section from WT mice at day 60 p.i., where DAPI is in blue, and A2B5 is in green. (I) represents the corpus callosum region of the brain section from NOS2-/- mice at day 60 p.i., where DAPI is in blue, and A2B5 is in green. (H-J) represent the white box in the corpus callosum region of the brain of WT and NOS2-/- mice, respectively, indicating $A2B5^+$ cells with a white arrow. Scale bar 25 µm,10 µm. (E and F) represent corresponding immunoblot and quantification graph of CNPase protein in RSA59-infected WT and NOS2-/- mouse-brain at day 60 p.i. (K and L) represent the corresponding immunoblot and quantification graph of PDGF-R protein in RSA59-infected WT and NOS2-/- mouse brain at day 60 p.i. Mean ± SEM was used to express results (n = 4-6 per group). *P < 0.05 was considered significant; asterisks indicate statistical significance determined using the unpaired Student's t-test plus Welch correction. *P < 0.05, **P < 0.01, ***P < 0.001, ****P < 0.0001.


IHC_Iba1Staining_Day-30
A.
WT
B.
NOS2-/-
C.
D.
E.
Percentage of Iba1-positive area of the brain at 30 dpi
% of Iba1 positive area
WT_30
NOS2-/-_30
F.
WT
NOS2-/-
SSC-A
CD45hiCD11b+
G. Infiltrating myeloid cell
Absolute number of cell
H.
CD45loCD11b+
I. CNS-resident microglia
ns
J.
CD45hiCD11b+CD68+
K.
CD45loCD11b+CD68+
L. CD68-expressing infiltrating myeloid cells
M. CD68-expressing CNS resident microglia

763

764

Figure-8 NOS2 deficiency leads to increased accumulation of activated microglia and peripheral myeloid cells in brain: 5 µm thick mid-sagittal brain sections of RSA59-infected (10,000 PFUs) WT and NOS2-/- mice were stained with anti-Iba1 antibody at day 30 p.i. (A) represents the brain of RSA59-infected WT mice. (B) represents the brain of RSA59-infected NOS2-/- mice. (C and D) represent the blue boxes of WT and NOS2-/- brain, respectively. Blue-boxed areas represent the higher-magnification images shown beside the corresponding brain section. (E) Quantification graph of the percentage of Iba1-positive area. Flow cytometry analysis was performed from brains of RSA59-infected WT and NOS2-/- mice at day 30 p.i. (F) represents corresponding plots of flow cytometry showing percentages of overall $CD45^{hi}$ $CD11b^{+}$ (infiltrating myeloid cell) population from WT and NOS2-/- mice after gating on live cells, followed by singlets. (G) Absolute cell numbers of CD45hi $CD11b^{+}$cell population from RSA59-infected WT and NOS2-/- mice. (H) represents corresponding plots of flow cytometry showing percentages of overall $CD45^{lo}$ $CD11b^{+}$ (CNS-resident microglia) cell population from WT and NOS2-/- mice after gating on live cells, followed by singlets. (I) Absolute cell numbers of $CD45^{lo}CD11b^{+}$cell population from RSA59 infected WT and NOS2-/- mice. (J and K) represent corresponding plot of flow cytometry indicating percentages of $CD45^{hi}CD11b^{+}$ cells and $CD45^{lo}$ $CD11b^{+}$ cells expressing CD68, comparing RSA59-infected WT and NOS2-/- mice. (L) Absolute cell numbers of CD68-positive cells within the $CD45^{hi}$ $CD11b^{+}$ cell population from RSA59-infected WT and NOS2-/- mice. (M) Absolute cell numbers of CD68-positive cells in the $CD45^{lo}$ $CD11b^{+}$ cell population from RSA59-infected WT and NOS2-/- mice. Scale bar 200 µm and 100 µm. Mean ± SEM was used to express the results (n = 4-5 per group). Asterisks indicate statistical significance, which was determined using an unpaired Student's t-test with Welch's correction; $P < 0.05$ was regarded as significant. ****$P < 0.0001$, **$P < 0.01$, and ***$P < 0.001$.

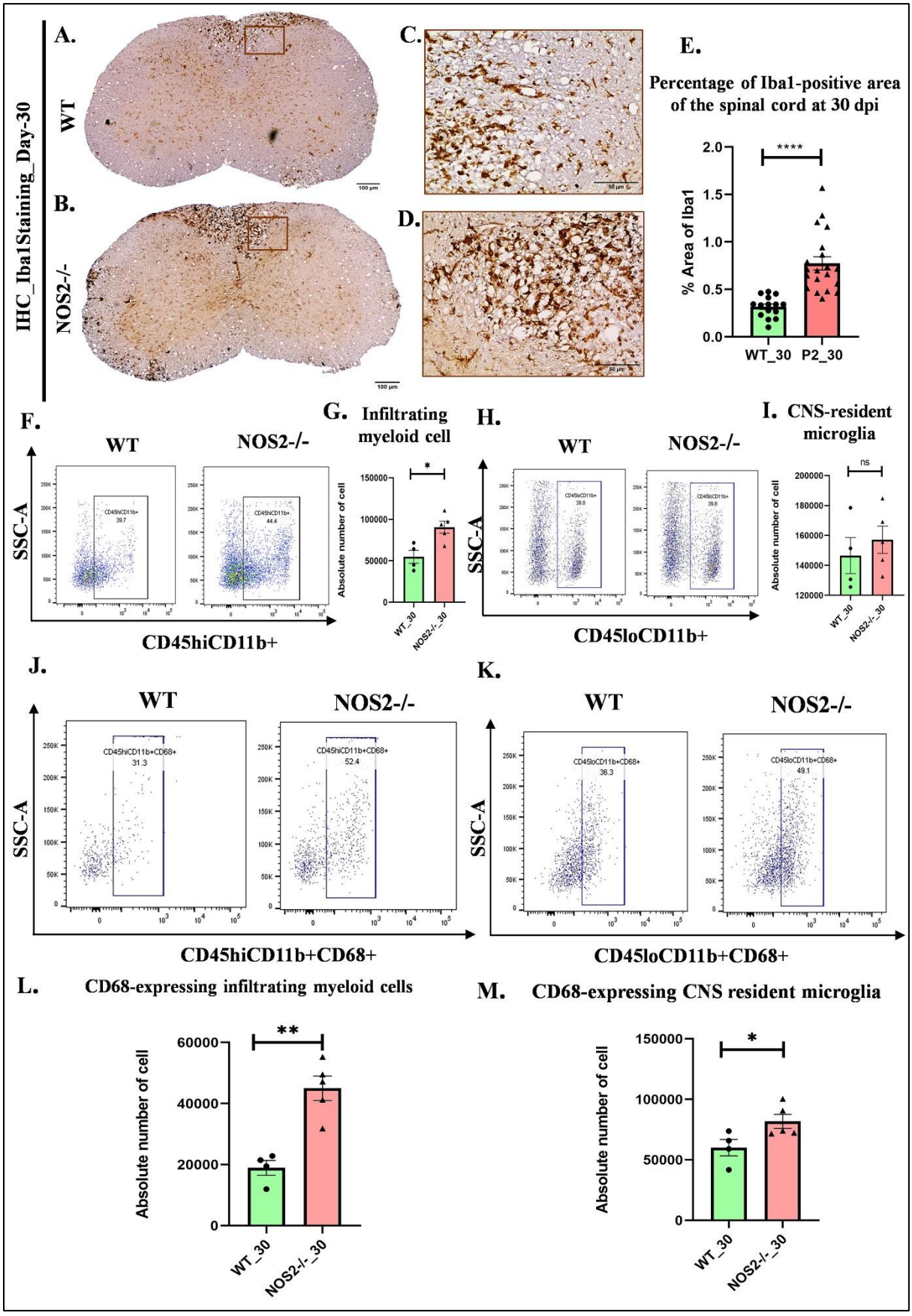
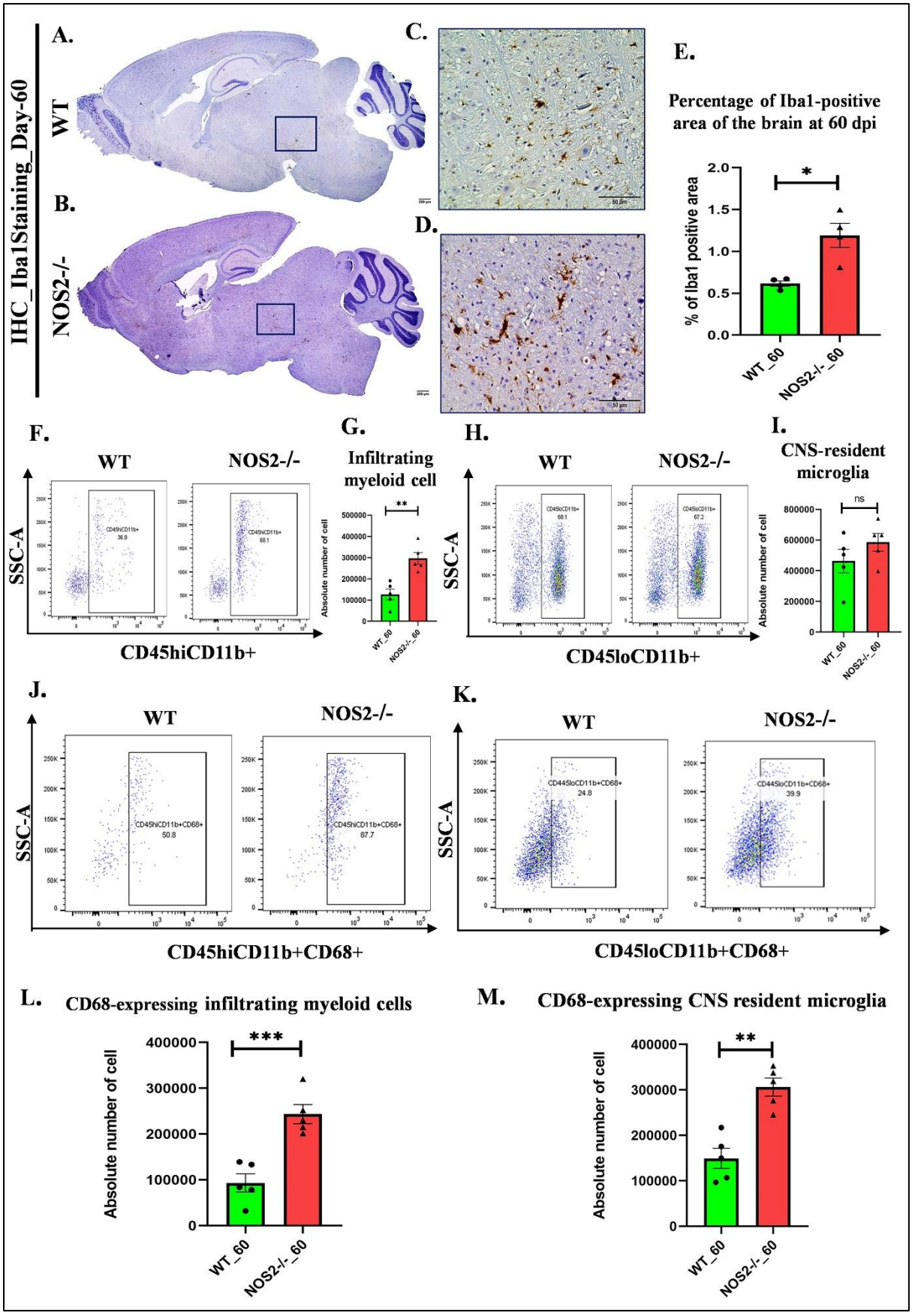

IHC_Iba1Staining_Day-30
A.
WT
B.
NOS2-/-
C.
D.
E.
Percentage of Iba1-positive area of the spinal cord at 30 dpi
% Area of Iba1
****
WT_30
P2_30
F.
WT
NOS2-/-
SSC-A
CD45hiCD11b+
G. Infiltrating myeloid cell
Absolute number of cell
*
H.
CD45loCD11b+
I. CNS-resident microglia
ns
J.
CD45hiCD11b+CD68+
K.
CD45loCD11b+CD68+
L. CD68-expressing infiltrating myeloid cells
**
M. CD68-expressing CNS resident microglia

Figure 9. NOS2 deficiency causes increased accumulation of activated microglia and peripheral myeloid cells in spinal cord: 5 μm-thick transverse spinal cord sections of RSA59-infected (10,000 PFUs) WT and NOS2-/- mice were stained with anti-Iba1 antibody at day 30 p.i. (A) represents the spinal cord of RSA59-infected WT mice. (B) represents the spinal-cord of RSA59-infected NOS2-/- mice. (C and D) represent the blue boxes of WT and NOS2-/- spinal cord, respectively. Blue-boxed areas represent the higher-magnification images shown beside the corresponding spinal-cord section. (E) Quantification graph of the percentage of Iba1-positive area. Flow cytometry analysis was performed from spinal-cords of RSA59-infected WT and NOS2-/- mice at day 30 p.i. (F) represents corresponding plots of flow cytometry showing percentages of overall $CD45^{hi}$ $CD11b^{+}$ (infiltrating myeloid cell) population from WT and NOS2-/- mice. (G) Absolute number of $CD45^{hi}$ $CD11b^{+}$ population from RSA59-infected WT and NOS2-/- mice. (H) represents corresponding plots of flow cytometry showing percentages of overall $CD45^{lo}$ CD11b+ (CNS-resident microglia) population from WT and NOS2-/- mice. (I) Absolute number of $CD45^{lo}CD11b^{+}$ population from RSA59-infected WT and NOS2-/- mice. (J and K) represent corresponding plots of flow cytometry indicating percentages of $CD45^{hi}CD11b^{+}$cells and $CD45^{lo}CD11b^{+}$ cells expressing CD68, comparing RSA59-infected WT and NOS2-/- mice. (L-M) represent absolute number of $CD68^{+}$ cells within the $CD45^{hi}CD11b^{+}$cell population and $CD45^{lo}$ $CD11b^{+}$ cell population respectively, from RSA59-infected WT and NOS2-/- mice. Scale bar 100 μm and 50 μm. One to six sections from various spinal cord regions were examined for the immunohistochemistry experiment (n = 4 per group); each dot in the graph represents one section from a single spinal cord. Each group in the flow cytometric experiment had n = 4-5. The mean ± SEM was used to express the results. Asterisks indicate statistical significance, which was determined by an unpaired Student's t-test with Welch correction; $P < 0.05$ was regarded as significant. **$P < 0.01$, ***$P < 0.001$, and ****$P < 0.0001$.


IHC_Iba1Staining_Day-60
A.
WT
B.
NOS2-/-
C.
D.
E.
Percentage of Iba1-positive area of the brain at 60 dpi
% of Iba1 positive area
WT_60
NOS2-/-_60
F.
WT
NOS2-/-
SSC-A
CD45hiCD11b+
G.
Infiltrating myeloid cell
Absolute number of cell
H.
CD45loCD11b+
I.
CNS-resident microglia
ns
J.
CD45hiCD11b+CD68+
K.
CD45loCD11b+CD68+
L.
CD68-expressing infiltrating myeloid cells
M.
CD68-expressing CNS resident microglia

828

Figure 10. NOS2 deficiency leads to enhanced number of phagocytic microglia and peripheral myeloid cells in brain: 5 µm mid-sagittal brain sections of RSA59-infected (10,000 PFUs) WT and NOS2-/- mice were stained with anti-Iba1 antibody at day 60 p.i. (A) represents the brain of RSA59-infected WT mice. (B) represents the brain of RSA59-infected NOS2-/- mice. (C and D) represent the blue boxes of WT and NOS2-/- brain, respectively. Blue-boxed areas represent the higher-magnification images shown beside the corresponding brain section. (E) Quantification graph of the percentage of Iba1-positive area. Brains from RSA59-infected WT and NOS2-/- mice were harvested for flow cytometry analysis and stained for CD45, CD11b, and CD68 at day 60 p.i. (F) represents corresponding plots of flow cytometry showing percentages of overall $CD45^{hi}$ $CD11b^{+}$ (infiltrating myeloid cell) population from WT and NOS2-/- mice after gating on live cells, followed by singlets. (G) Absolute cell numbers of $CD45^{hi}$ $CD11b^{+}$population from RSA59-infected WT and NOS2-/- mice. (H) represents corresponding plots of flow cytometry showing percentages of overall $CD45^{lo}CD11b^{+}$(CNS-resident microglia) cell population from WT and NOS2-/- mice after gating on live cells, followed by singlets. (I) Absolute cell numbers of $CD45^{lo}CD11b^{+}$cell population from RSA59-infected WT and NOS2-/- mice. (J and K) represent corresponding plots of flow cytometry indicating percentages of $CD45^{hi}CD11b^{+}$ cells and $CD45^{lo}$ $CD11b^{+}$ cells expressing CD68, comparing RSA59-infected WT and NOS2-/- mice. (L) Absolute cell numbers of CD68-positive cells within the $CD45^{hi}$ $CD11b^{+}$ cell population from RSA59-infected WT and NOS2-/- mice. (M) Absolute cell numbers of CD68-positive cells in the CD45lo CD11b+ cell population from RSA59-infected WT and NOS2-/- mice. Scale bar:200 µm,100 µm. The mean ± SEM was used to express the results (n = 4-5 per group). Asterisks indicate statistical significance, which was determined by an unpaired Student's t-test with Welch correction; $P < 0.05$ was regarded as significant. **$P < 0.01$, ***$P < 0.001$, and ****$P < 0.0001$.

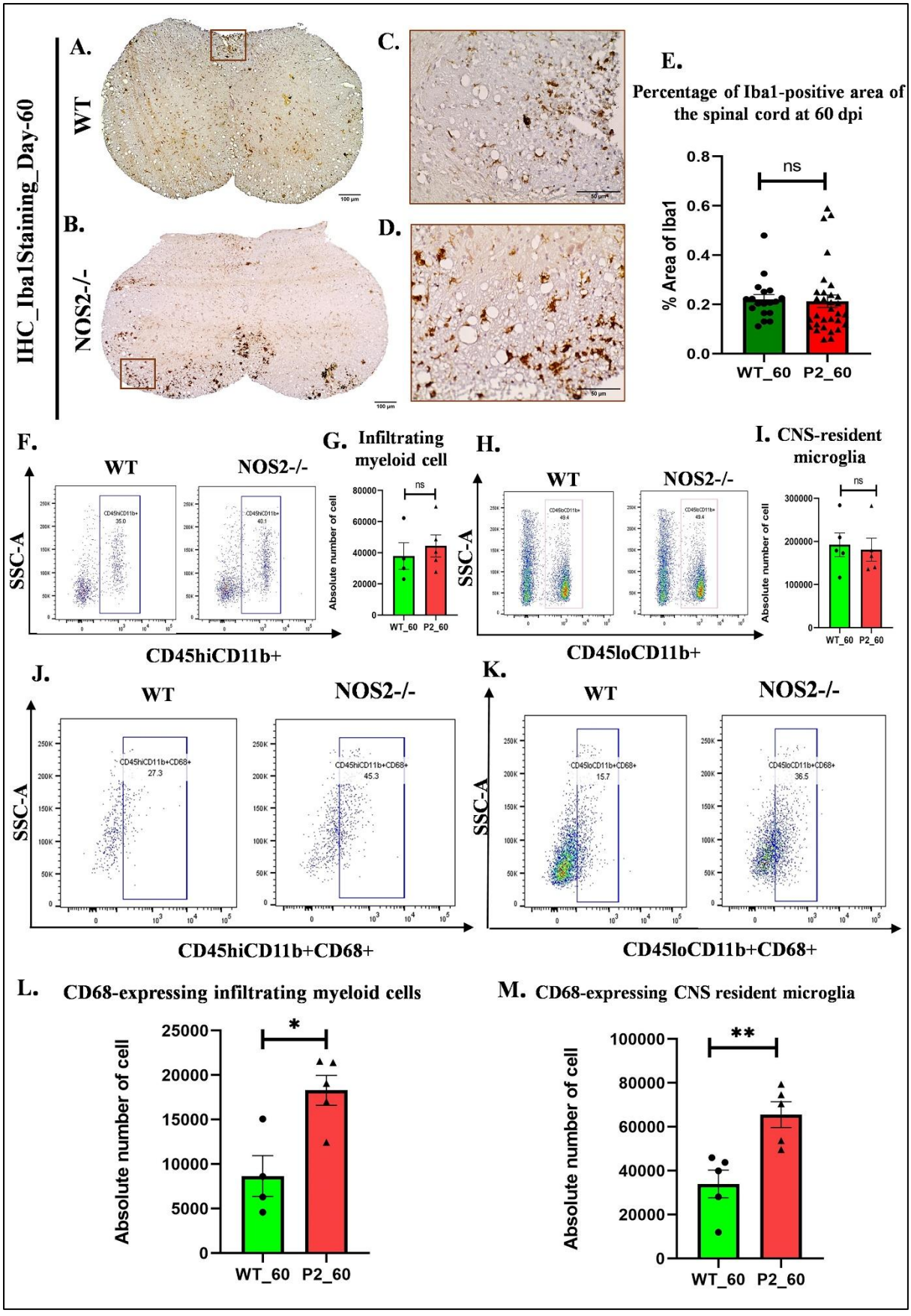

IHC_Iba1Staining_Day-60
A.
WT
B.
NOS2-/-
C.
D.
E.
Percentage of Iba1-positive area of the spinal cord at 60 dpi
% Area of Iba1
ns
WT_60
P2_60
F.
WT
NOS2-/-
SSC-A
CD45hiCD11b+
G. Infiltrating myeloid cell
Absolute number of cell
H.
CD45loCD11b+
I. CNS-resident microglia
J.
CD45hiCD11b+CD68+
K.
CD45loCD11b+CD68+
L. CD68-expressing infiltrating myeloid cells
M. CD68-expressing CNS resident microglia
*
**

Figure 11. NOS2 deficiency leads to exacerbated phagocytic microglia and peripheral myeloid cells in the spinal cord: 5 µm transverse spinal cord sections of RSA59-infected (10,000 PFUs) WT and NOS2-/- mice were stained with anti-Iba1antibody at day 60 p.i. (A-B) represent the spinal cord of RSA59-infected WT mice and NOS2-/- mice respectively. (C and D) represent the blue boxes of WT and NOS2-/- spinal cord, respectively. Blue-boxed areas represent higher-magnification images shown beside the corresponding spinal cord section. (E) Quantification graph of the percentage of Iba1-positive area. Flow cytometry analysis was performed on spinal cords of RSA59-infected WT and NOS2-/- mice at day 30 p.i. (F) represents corresponding plots of flow cytometry showing percentages of overall $CD45^{hi}$ $CD11b^{+}$ (infiltrating myeloid cell) population from WT and NOS2-/- mice. (G) Absolute cell numbers of $CD45^{hi}$ $CD11b^{+}$ population from RSA59-infected WT and NOS2-/- mice. (H) represents corresponding plots of flow cytometry showing percentages of overall $CD45^{lo}$ $CD11b^{+}$ (CNS-resident microglia) population from WT and NOS2-/- mice. (I) Absolute cell numbers of $CD45^{lo}CD11b^{+}$ population from RSA59-infected WT and NOS2-/- mice. (J-K) represent corresponding plots of flow cytometry indicating percentages of $CD45^{hi}CD11b^{+}$ and $CD45^{lo}CD11b^{+}$ cell population expressing CD68 comparing RSA59-infected WT and NOS2-/- mice. (L-M) represent absolute cell numbers of $CD68^{+}$ cells within $CD45^{hi}CD11b^{+}$cell population and $CD45^{lo}$ $CD11b^{+}$ cell population respectively, from RSA59-infected WT and NOS2-/- mice. Scale bar 100 µm and 50 µm. Each dot in the graph represents a section from a single spinal cord. For immunohistochemistry experiment, n = 4-6 per group; 1- 6 sections corresponding to various spinal cord regions were evaluated. n = 4-5 for each group in the flow cytometric assay. Mean ± SEM was used to express the results. * Asterisks indicate statistical significance, which was determined by unpaired Student's t-test with Welch correction; $P < 0.05$ was regarded as significant. *$P < 0.05$, **$P < 0.01$, ***$P < 0.001$, ****$P < 0.0001$, and ns-not significant.

Declarations:

Ethics Approval and Consent to Participate: All animal procedures were conducted in compliance with institutional ethical guidelines and were approved by the Institutional Animal Ethics Committee (Protocol numbers IISERK/IAEC/AP/2024/125 and IISERK/IAEC/AP/2019/45 were used in this study). No human subjects were involved in this study. Experiments were performed in accordance with the guidelines of the Committee for Control and Supervision of Experiments on Animals (CCSEA), India.

Availability of Data and Materials: The data supporting the study findings are available from the corresponding author upon request.

Competing Interests: The authors declare no competing interests.

Funding: This work was supported by the DBT Emerging Frontiers in Biotechnology (Grant No: BT/PR56534/BMS2/156/125/2024), Anusandhan National Research Foundation (ANRF) Core Grant, SERB, India (Grant No: CRG/2023/000999) and internal support from IISER Kolkata.

Authors' Contributions:

Rishika Jana: Conceptualization, Data curation, Formal analysis, Investigation, Methodology, Software, Visualization, Writing - original draft, Writing -editing

Santosh Kumar Samal: Methodology, Data curation, Formal analysis

Souvik Karmakar: Methodology, Data curation, Formal analysis

Subhajit Das Sarma: Methodology

Jayasri Das Sarma: Conceptualization, Formal analysis, Funding acquisition, Investigation, Project administration, Resources, Supervision, Validation, Visualization, Writing – original draft, Writing – review & editing

Acknowledgments:

We acknowledge the support of the Department of Biological Sciences, the State-of-the-Art Animal Facility and Central Imaging Facility at IISER Kolkata, and the Intramural and Academic Research Fund of IISER Kolkata. The authors gratefully acknowledge Dr. Judith B. Grinspan (CHOP, Philadelphia) for the PLP, MBP, and A2B5 antibodies. We would also like to acknowledge the Department of Science and Technology-Innovation in Science Pursuit for Inspired Research (INSPIRE) for providing a fellowship to RJ, and the Council for Scientific and Industrial Research (CSIR) for providing fellowships to SKS and SK. We thank Ms. Satavisha Ghosh and Mr. Bishal Hazra for their help in the flow cytometry data acquisition.

References:

1. Filippi M, Bar-Or A, Piehl F, Preziosa P, Solari A, Vukusic S, et al. Multiple sclerosis. Nat Rev Dis Primers. Nature Publishing Group; 2018;4. https://doi.org/10.1038/s41572-018-0041-4

2. Frischer JM, Weigand SD, Guo Y, Kale N, Parisi JE, Pirko I, et al. Clinical and pathological insights into the dynamic nature of the white matter multiple sclerosis plaque. Ann Neurol. John Wiley and Sons Inc.; 2015; 78:710–21. https://doi.org/10.1002/ana.24497

3. Dendrou CA, Fugger L, Friese MA. Immunopathology of multiple sclerosis. Nat. Rev. Immunol. Nature Publishing Group; 2015. p. 545–58. https://doi.org/10.1038/nri3871

4. Smolders J, Hsiao CC, Huitinga I, Hamann J. Resident T cells in the healthy and multiple sclerosis brain. Trends Immunol. Elsevier Ltd; 2026. https://doi.org/10.1016/j.it.2025.12.006

5. Ferguson B. Axonal damage in acute multiple sclerosis lesions. Brain. 1997; 120:393–9. https://doi.org/10.1093/brain/120.3.393

6. Catherine Lubetzki 1 *, Bruno Stankoff 1. Demyelination in multiple sclerosis. 2014. p. 89–99. https://doi.org/10.1016/B978-0-444-52001-2.00004-2

7. Traka M, Podojil JR, Mccarthy DP, Miller SD, Popko B. Oligodendrocyte death results in immune-mediated CNS demyelination. Nat Neurosci. Nature Publishing Group; 2015; 19:65–74. https://doi.org/10.1038/nn.4193

8. Ozawa K, Suchanek G, Breitschopf H, Brück W, Budka H, Jellinger K, Lassmann H. Patterns of oligodendroglia pathology in multiple sclerosis. Brain. 1994; 117:1311–22. https://doi.org/10.1093/brain/117.6.1311

9. Peterson LK, Fujinami RS. Inflammation, demyelination, neurodegeneration and neuroprotection in the pathogenesis of multiple sclerosis. J. Neuroimmunol. 2007. p. 37–44. https://doi.org/10.1016/j.jneuroim.2006.11.015

10. Frischer JM, Bramow S, Dal-Bianco A, Lucchinetti CF, Rauschka H, Schmidbauer M, et al. The relation between inflammation and neurodegeneration in multiple sclerosis brains. Brain. 2009; 132:1175–89. https://doi.org/10.1093/brain/awp070

11. Mahajan KR, Herman D, Zheng Y, Androjna C, Thoomukuntla B, Ontaneda D, et al. Neurodegeneration and Demyelination in the Multiple Sclerosis Spinal Cord: Clinical,

948 Pathological, and 7T MRI Perspectives. Neurology. Lippincott Williams and Wilkins;
949 2025;104. https://doi.org/10.1212/WNL.0000000000210259

950 12. Ruiz F, Vigne S, Pot C. Resolution of inflammation during multiple sclerosis. Semin.
951 Immunopathol. Springer; 2019. p. 711–26. https://doi.org/10.1007/s00281-019-00765-0

952 13. Goldschmidt C, McGinley MP. Advances in the Treatment of Multiple Sclerosis. Neurol.
953 Clin. W.B. Saunders; 2021. p. 21–33. https://doi.org/10.1016/j.ncl.2020.09.002

954 14. Garcha GK, Ahmed M. Remyelination as a therapeutic target in the treatment of multiple
955 sclerosis. AIMS Neurosci. 2025 Nov 6;12(4):539-
956 569. https://doi.org/10.3934/Neuroscience.2025027

957 15. Franklin RJM, Ffrench-Constant C. Regenerating CNS myelin - From mechanisms to
958 experimental medicines. Nat. Rev. Neurosci. Nature Publishing Group; 2017. p. 753–69.
959 https://doi.org/10.1038/nrn.2017.136

960 16. Franklin RJM, Ffrench-Constant C. Remyelination in the CNS: From biology to therapy.
961 Nat. Rev. Neurosci. 2008. p. 839–55. https://doi.org/10.1038/nrn2480

962 17. Steinman L. Multiple Sclerosis: A Coordinated Review Immunological Attack against
963 Myelin in the Central Nervous System. Cell. 1996.

964 18. Høglund RA. Multiple sclerosis and the role of immune cells. World J Exp Med. 2014;
965 4:27. https://doi.org/10.5493/wjem.v4.i3.27

966 19. Martin R, McFarland HF, McFarlin DE. Immunological Aspects of Demyelinating
967 Diseases. Annu Rev Immunol. 1992; 10:153–87.
968 https://doi.org/10.1146/annurev.iy.10.040192.001101

969 20. Prinz M, Masuda T, Wheeler MA, Quintana FJ. Microglia and Central Nervous System-
970 Associated Macrophages-From Origin to Disease Modulation. Annu Rev Immunol. 2021. p.
971 251–77. https://doi.org/10.1146/annurev-immunol-093019-110159

972 21. Hyvärinen T, Tilvis J, Giudice L, Tujula I, Nylund M, Ohtonen S, et al. Microglia from
973 patients with multiple sclerosis display a cell-autonomous immune activation state. Journal of
974 Neuroinflammation. BioMed Central Ltd; 2025;22. https://doi.org/10.1186/s12974-025-
975 03575-4

22. Das Sarma J. Microglia-mediated neuroinflammation is an amplifier of virus-induced neuropathology. J Neurovirol. 2014 Apr;20(2):122-36. https://doi.org/10.1007/s13365-013-0188-4

23. Sherafat A, Pfeiffer F, Reiss AM, Wood WM, Nishiyama A. Microglial neuropilin-1 promotes oligodendrocyte expansion during development and remyelination by trans-activating platelet-derived growth factor receptor. Nat Commun. Nature Research; 2021;12. https://doi.org/10.1038/s41467-021-22532-2

24. Sariol A, Mackin S, Allred M-G, Ma C, Zhou Y, Zhang Q, et al. Microglia depletion exacerbates demyelination and impairs remyelination in a neurotropic coronavirus infection. Proceedings of the National Academy of Sciences. 2020; 117:24464–74. https://doi.org/10.1073/pnas.2007814117

25. Smith KJ, Lassmann H. The role of nitric oxide in multiple sclerosis. Lancet Neurol. 2002; 1:232–41. https://doi.org/10.1016/S1474-4422(02)00102-3

26. Bogdan C. Nitric oxide synthase in innate and adaptive immunity: An update. Trends Immunol. Elsevier Ltd; 2015. p. 161–78. https://doi.org/10.1016/j.it.2015.01.003

27. Hill KE, Zollinger L V., Watt HE, Carlson NG, Rose JW. Inducible nitric oxide synthase in chronic active multiple sclerosis plaques: Distribution, cellular expression and association with myelin damage. J Neuroimmunol. 2004; 151:171–9. https://doi.org/10.1016/j.jneuroim.2004.02.005

28. Raposo C, Nunes AK, Luna RL, Araújo SM, da Cruz-Höfling MA, Peixoto CA. Sildenafil (Viagra) protective effects on neuroinflammation: the role of iNOS/NO system in an inflammatory demyelination model. Mediators Inflamm. 2013.;2013:321460. https://doi.org/10.1155/2013/321460

29. Cross AH, Misko TP, Lin RF, Hickey WF, Trotter JL, Tilton RG. Aminoguanidine, an inhibitor of inducible nitric oxide synthase, ameliorates experimental autoimmune encephalomyelitis in SJL mice. J Clin Invest. 1994 Jun;93(6):2684-90. doi: 10.1172/JCI117282.

30. Sahrbacher UC, Lechner F, Eugster HP, Frei K, Lassmann H, Fontana A. Mice with an inactivation of the inducible nitric oxide synthase gene are susceptible to experimental

1005 autoimmune encephalomyelitis. Eur J Immunol. 1998 Apr;28(4):1332-8. doi:
1006 10.1002/(SICI)1521-4141(199804)28:04<1332::AID-IMMU1332>3.0.CO;2-G.

1007 31. Zhong J, Yau ACY, Holmdahl R. Independent and inter-dependent immunoregulatory
1008 effects of NCF1 and NOS2 in experimental autoimmune encephalomyelitis. J
1009 Neuroinflammation. BioMed Central Ltd.; 2020;17. https://doi.org/10.1186/s12974-020-
1010 01789-2

1011 32. Fenyk-Melody JE, Garrison AE, Brunnert SR, Weidner JR, Shen F, Shelton BA, Mudgett
1012 JS. Experimental autoimmune encephalomyelitis is exacerbated in mice lacking the NOS2
1013 gene. J Immunol. 1998 Mar 15;160(6):2940-6.

1014 33. Lane TE, Fox HS, Buchmeier MJ. Inhibition of nitric oxide synthase-2 reduces the severity
1015 of mouse hepatitis virus-induced demyelination: Implications for NOS2/NO regulation of
1016 chemokine expression and inflammation. J Neurovirol. Nature Publishing Group; 1999; 5:48–
1017 54. https://doi.org/10.3109/13550289909029745

1018 34. Chen BP, Lane TE. Lack of nitric oxide synthase type 2 (NOS2) results in reduced neuronal
1019 apoptosis and mortality following mouse hepatitis virus infection of the central nervous system.
1020 J Neurovirol. 2002 Feb;8(1):58-63. doi: 10.1080/135502802317247820.

1021 35. Wu GF, Pewe L, Perlman S. Coronavirus-induced demyelination occurs in the absence of
1022 inducible nitric oxide synthase. J Virol. 2000 Aug;74(16):7683-6. doi: 10.1128/jvi.74.16.7683-
1023 7686.2000.

1024 36. Das Sarma J. A mechanism of virus-induced demyelination. Interdiscip Perspect Infect Dis.
1025 2010; 2010:109239. doi: 10.1155/2010/109239.

1026 37. Saadi F, Chakravarty D, Kumar S, Kamble M, Saha B, Shindler KS, Das Sarma J. CD40L
1027 protects against mouse hepatitis virus-induced neuroinflammatory demyelination. PLoS
1028 Pathog. Public Library of Science; 2021;17. https://doi.org/10.1371/journal.ppat.1010059

1029 Kamble M, Saadi F, Kumar S, Saha B, Das Sarma J. Inducible nitric oxide synthase deficiency
1030 promotes murine-β-coronavirus induced demyelination. Virol J. 2023 Mar 25;20(1):51.
1031 https://doi.org/10.1186/s12985-023-02006-1

1032 39. Das Sarma J, Scheen E, Seo SH, Koval M, Weiss SR. Enhanced green fluorescent protein
1033 expression may be used to monitor murine coronavirus spread in vitro and, in the mouse,

central nervous system. J Neurovirol. 2002 Oct;8(5):381-91. https://doi.org/10.1080/13550280290100815

40. Laubach VE, Shesely EG, Smithies O, Sherman PA. Mice lacking inducible nitric oxide synthase are not resistant to lipopolysaccharide-induced death. Proc Natl Acad Sci U S A. 1995 Nov 7;92(23):10688-92. doi: 10.1073/pnas.92.23.10688.

41. Chakravarty D, Saadi F, Kundu S, Bose A, Khan R, Dine K, Kenyon LC, Shindler KS, Das Sarma J. CD4 Deficiency Causes Poliomyelitis and Axonal Blebbing in Murine Coronavirus-Induced Neuroinflammation. J Virol. American Society for Microbiology; 2020;94. https://doi.org/10.1128/jvi.00548-20

42. Wheeler DL, Sariol A, Meyerholz DK, Perlman S. Microglia are required for protection against lethal coronavirus encephalitis in mice. Journal of Clinical Investigation. American Society for Clinical Investigation; 2018; 128:931–43. https://doi.org/10.1172/JCI97229

43. Goodman ZD. Grading and staging systems for inflammation and fibrosis in chronic liver diseases. J. Hepatol. 2007. p. 598–607. https://doi.org/10.1016/j.jhep.2007.07.006

44. Singh M, Kishore A, Maity D, Sunanda P, Krishnarjuna B, Vappala S, Raghothama S, Kenyon LC, Pal D, Das Sarma J. A proline insertion-deletion in the spike glycoprotein fusion peptide of mouse hepatitis virus strongly alters neuropathology. J Biol Chem. 2019 May 17;294(20):8064-8087. https://doi.org/10.1074/jbc.RA118.004418

45. Sharma M, Chakravarty D, Hussain A, Zalavadia A, Burrows A, Rayman P, Sharma N, Kenyon LC, Bergmann C, Sen GC, Das Sarma J. Ifit2 restricts murine coronavirus spread to the spinal cord white matter and its associated myelin pathology. J Virol. 2023 Aug 31;97(8): e0074923.https://doi.org/10.1128/jvi.00749-23

46. Karmakar S, Das Sarma J. Human coronavirus OC43 infection remodels connexin 43-mediated gap junction intercellular communication *in vitro*. J Virol. 2024;98. https://doi.org/10.1128/jvi.00478-24

47. Ghosh S, Jana R, Jana S, Basu R, Chatterjee M, Ranawat N, Das Sarma J. Differential expression of cellular prion protein (PrP^C) in mouse hepatitis virus induced neuroinflammation. J Neurovirol. 2024 Jun;30(3):215-228. https://doi.org/10.1007/s13365-024-01215-w

48. Das Sarma J, Burrows A, Rayman P, Hwang MH, Kundu S, Sharma N, Bergmann C, Sen GC. Ifit2 deficiency restricts microglial activation and leukocyte migration following murine

coronavirus (m-CoV) CNS infection. PLoS Pathog. 2020 Nov 30;16(11): e1009034.https://doi.org/10.1371/journal.ppat.1009034

49. Fulton D, Paez PM, Campagnoni AT. The multiple roles of myelin protein genes during the development of the oligodendrocyte. ASN Neuro. 2010. p. 25–37. https://doi.org/10.1042/AN20090051

50. Jana M, Ghosh S, Pahan K. Upregulation of Myelin Gene Expression by a Physically-Modified Saline via Phosphatidylinositol 3-Kinase-Mediated Activation of CREB: Implications for Multiple Sclerosis. Neurochem Res. Springer New York LLC; 2018;43:407–19. https://doi.org/10.1007/s11064-017-2435-1

51. Shiota C, Miura M, Mikoshiba K. Developmental profile and differential localization of mRNAs of myelin proteins (MBP and PLP) in oligodendrocytes in the brain and in culture. Brain Res Dev Brain Res. 1989 Jan 1;45(1):83-94. doi: 10.1016/0165-3806(89)90010-2.

52. Baumann N, Pham-Dinh D. Biology of oligodendrocyte and myelin in the mammalian central nervous system. Physiol Rev. 2001 Apr;81(2):871-927. doi: 10.1152/physrev.2001.81.2.871.

53. Mitew S, Hay CM, Peckham H, Xiao J, Koenning M, Emery B. Mechanisms regulating the development of oligodendrocytes and central nervous system myelin. Neuroscience. 2014 Sep 12; 276:29-47. https://doi.org/10.1016/j.neuroscience.2013.11.029

54. Franklin RJ, Goldman SA. Glia Disease and Repair-Remyelination. Cold Spring Harb Perspect Biol. 2015 May 18;7(7): a020594.https://doi.org/10.1101/cshperspect.a020594

55. Young KM, Psachoulia K, Tripathi RB, Dunn SJ, Cossell L, Attwell D, Tohyama K, Richardson WD. Oligodendrocyte dynamics in the healthy adult CNS: evidence for myelin remodeling. Neuron. 2013 Mar 6;77(5):873-85. https://doi.org/10.1016/j.neuron.2013.01.006

56. Lampron A, Larochelle A, Laflamme N, Préfontaine P, Plante MM, Sánchez MG, Yong VW, Stys PK, Tremblay MÈ, Rivest S. Inefficient clearance of myelin debris by microglia impairs remyelinating processes. J Exp Med. 2015 Apr 6;212(4):481-95. https://doi.org/10.1084/jem.20141656

57. McCallum S, Suresh KB, Islam TS, Tripathi MK, Saustad AW, Shelest O, Patil A, Lee D, Kwon B, Leitholf K, Yenokian I, Shaka SE, Beveridge CH, Manchandra P, Randolph CE, Meares GP, Dutta R, Plummer J, Calsavara VF, Kawaguchi R, Knott SRV, Chopra G, Burda

JE. Lesion-remote astrocytes govern microglia-mediated white matter repair. Nature. 2026 Jan;649(8098):959-970. https://doi.org/10.1038/s41586-025-09887-y

58. Mishra MK, Rawji KS, Keough MB, Kappen J, Dowlatabadi R, Vogel HJ, Chopra S, Distéfano-Gagné F, Dufour A, Gosselin D, Yong VW. Harnessing the Benefits of Neuroinflammation: Generation of Macrophages/Microglia with Prominent Remyelinating Properties. J Neurosci. 2021 Apr 14;41(15):3366-3385. https://doi.org/10.1523/JNEUROSCI.1948-20.2021

59. Cignarella F, Filipello F, Bollman B, Cantoni C, Locca A, Mikesell R, Manis M, Ibrahim A, Deng L, Benitez BA, Cruchaga C, Licastro D, Mihindukulasuriya K, Harari O, Buckland M, Holtzman DM, Rosenthal A, Schwabe T, Tassi I, Piccio L. TREM2 activation on microglia promotes myelin debris clearance and remyelination in a model of multiple sclerosis. Acta Neuropathol. 2020 Oct;140(4):513-534.https://doi.org/10.1007/s00401-020-02193-z

60. Hammel G, Zivkovic S, Ayazi M, Ren Y. Consequences and mechanisms of myelin debris uptake and processing by cells in the central nervous system. Cell Immunol. 2022 Oct; 380:104591. https://doi.org/10.1016/j.cellimm.2022.104591

1121

1122

1123

1124

1125

1126

1127

1128

1129